THESIS FOR THE DEGREE OF LICENTIATE OF ENGINEERING

Sustainable Energy Conversion from Biomass Waste Combustion

Particle Modelling and Experimental Studies

Maulana Nugraha

Chemical Engineering Division
Department of Chemistry and Chemical Engineering

CHALMERS UNIVERSITY OF TECHNOLOGY

Gothenburg, Sweden 2019

Sustainable Energy Conversion from Biomass Waste Combustion
Particle Modelling and Experimental Studies

Maulana Nugraha

Licentiatuppsatser vid Institutionen för kemi och kemiteknik
Chalmers tekniska högskola.
Nr 2019:08

Department of Chemistry and Chemical Engineering
Chalmers University of Technology
SE-412 96 Gothenburg
Sweden
Telephone + 46 (0)31-772 1000

Printed by Chalmers Reproservice
Gothenburg, Sweden 2019

Sustainable Energy Conversion from Biomass Waste Combustion
Particle Modelling and Experimental Studies

Maulana Nugraha

Department of Chemistry and Chemical Engineering
Chalmers University of Technology, Gothenburg 2019

Abstract

Various biomass-type conversions into sustainable heat and power, from dedicated crops to solid biomass waste via the combustion process, are at the center of scientific and industrial focus today. However, biomass combustion contribution to global particulate matter (PM) emission has become one of the biggest challenges that remain in the development of sustainable biomass combustion systems. Particulate matter emission is well-known to be a strongly threatening agent to human health, causing 3.7 million premature deaths in 2012 according to the World Health Organization. Based on this fact, developing knowledge on how to reduce PM emission in biomass combustion systems is the main concern of this thesis. This work includes the development of models and experimental methods on different scales.

Designing an advanced biomass combustion furnace is the first step to developing the knowledge on a large scale. The constructed furnace allows detailed observation of different combustion parameters and PM characteristics. The furnace is fueled with waste biomass and equipped with a combination of a PM sampling system and accurate, real time, and flexible measurements of temperature and exhaust gas composition.

In order to produce more correct predictions of PM precursors, the development of a computationally efficient and accurate thermally thick particle model for a combustion system is performed on a smaller scale. Partial differential equations (PDEs) for heat and mass balance are transformed into ordinary differential equations (ODEs) with the utilization of orthogonal collocation as the particle discretization method. The transformation allows the current model to be implemented into the computational fluid dynamics (CFD) environment using sub-grid-scale modelling.

A detailed study of the effect of Stefan flow on particle surface using CFD analysis allows improvement of the boundary layer heat and mass transfer in particle modelling. The effect of Stefan flow is found to be pronounced since it reduces the oxidative gas mass transfer rate to the particle surface, and at the same time, it has significant effects on the convective heat flux from or to the bulk gas. The efficiency of the current particle model is demonstrated through the low usage of computational power. The employed particle model is also proven to be accurate and stable through its high degree of agreement with simulation results for particle pyrolysis and combustion experiments using different particle moisture contents, shapes, and sizes.

Keywords: biomass waste combustion, particulate matter, furnace, particle modelling, orthogonal collocation, computational fluid dynamics (CFD), Stefan flow.

Acknowledgements

The research presented in this thesis was conducted within Chemical Engineering Division at Chalmers University of Technology, Sweden and Chemical Engineering and Mechanical Engineering Department at Universitas Gadjah Mada (UGM), Indonesia. The financial support from the Swedish Research Council is gratefully acknowledged.

I would like to immensely thank many people who have supported me, in particular:

My supervisor, **Assoc. Prof. Ronnie Andersson**, who giving me the opportunity to be a PhD student within your research group. I am very thankful to have all the encouraging and intensive discussions with you. Your valuable advices really motivated me a lot to be a better researcher.

My co-supervisor, **Prof. Bengt Andersson**, for a lot of wonderful and valuable ideas during research discussions. You are really helping me to see broader perspective of things.

My co-supervisors in Indonesia, **Prof. Harwin Saptoadi** and **Assoc. Prof. Muslikhin Hidayat**, for massive supports to manage experimental works in UGM's lab.

My former office mates, **Mohsen** and **Soheil**. Thanks for making such a wonderful office. I am really enjoying all the joyful and encouraging discussions that we had.

All my current and former colleagues in KRT who offered not only a pleasant work atmosphere but also wonderful badminton, football, and UNO sessions.

All my former bachelor students in UGM, **Denny, Aziz, Ariq, Ali, Fuad, Qiqi** and **Wahyu**, who have helped me to run the experiments in Indonesia.

All current and former Indonesian student in Gothenburg, **Iqbaal, Mas Ferry, Mbak Nia, Pak Azis, Mas Luki** and many others, for all valuable help during staying in Sweden which making me feels really like in home.

My mother and **my father** for providing me with the opportunity to be where I am today. I love you so much. Also for my sister, **Mbak Dama**, who supported me and helped me throughout my life.

The ultimate thanks are contributed to the most important people in my life now. For my little daughter, **Khaylila**, thanks for made me stronger, better and more fulfilled than I could have ever imagined. I love you to the moon and back. For my beloved wife, **Anggi**, I love you for everything, for being so understanding and for putting up with me through the toughest moments of my life. I thank God for enlightening my life with your presence. You are the best thing that has ever happened to me.

List of Publications

This thesis is based on the work reported in the following papers, referred to by Roman numerals in the text :

Paper I

Particle Modelling in Biomass Combustion using Orthogonal Collocation
Maulana G. Nugraha, Harwin Saptoadi, Muslikhin Hidayat, Bengt Andersson, Ronnie Andersson
Submitted manuscript to Applied Energy

Paper II

Sherwood Number Correction for Stefan flow
Bengt Andersson, Maulana G. Nugraha, Ronnie Andersson
Manuscript

Contribution Report

The author of this thesis has made the following contributions to the included papers :

Paper I

Main author. I planned and conducted the modelling and simulation works. I wrote and submitted the manuscript. I analyzed the simulation results together with co-authors.

Paper II

Co-author. I planned the modelling and simulation works together with the main author and co-author. I analyzed the simulation results together with main author and co-author.

List of Abbreviations

BC	Boundary Condition
CFD	Computational Fluid Dynamics
COPD	Chronic Obstructive Pulmonary Disease
EU	European Union
LPG	Liquiefied Pertoleoum Gas
ODE	Oridinary Differential Equation
PDE	Partial Differential Equation
PM	Particulate Matter

Table of Contents

1. INTRODUCTION

1.1. Background

The rising demand for the worldwide energy and the concern for greenhouse gas emission has accelerated global interest in alternative energy conversion from biomass [1–4]. Various biomass-type conversions into sustainable heat and power, from dedicated crops to solid biomass waste, via the combustion process are at the center of scientific and industrial focus today [5–9]. Energy conversion from biomass is exploited in order to reach the target for renewable energy utilization that has been determined for some regions or countries, for example the EU, to be 27% in 2030 [10], and for Sweden to be 100% in 2040 [11] (% renewable energy from total energy production).

Biomass combustion is known to be a major source of outdoor particulate matter (PM) air pollution [12]. PM emission in ambient air contributes to 3.7 million premature death worldwide or 6.7% of all death cases in 2012. Moreover, PM from biomass combustion also contributes to climate change by absorbing and scattering sunlight. The carbonaceous compound in PM is known to absorb sunlight, and, consequently, contributes to more severe global warming. PM emission has also been found to influence cloud formation, which indirectly affects climate change worldwide [13].

The formation and removal of PM are considered as well-studied phenomena but still an active area of research today [14]. This is due to the complexity of PM formation pathway which is really determined by several combustion parameters i.e. parent fuel characteristics (size and chemical compositions) and combustion conditions (the mixing of air and fuel, the air fuel ratio, combustion temperature and gas residence time). The very broad variations of these factors create the difficulty in determining the valid scheme for PM formation in biomass combustion even numerous research have been conducted [15].

Development of CFD simulation methods, which are thoroughly validated using reliable data from experimental works, is believed to accelerate the understanding of PM formation and a step towards to PM reduction. Modeling the combustion system using CFD may involve biomass particle models. An accurate physicochemical particle model is crucial to forecast the correct PM precursor release, which leads to better prediction of PM formation pathway. Due to the scale-separation problem, i.e. order of magnitude differences between particles and the furnace, sub-grid models need to be developed. The particle model must also be stable and computational efficient to be implemented [16,17].

A successful model allows different operating conditions in the reactor to be evaluated by computer simulation, which may significantly reduce the number of costly experiments. Finally, the simulation methods may significantly help to find the optimum biomass combustion condition with the least PM emission in an accurate and efficient way.

1.2. Objectives

Based on the challenges in Background section, developing knowledge of PM reduction in biomass combustion system is the primary concern of the whole PhD project. However, in this work, the objectives are limited to the development of sub-grid scale biomass particle model and the development of a biomass combustion furnace to support the main goal.

Designing and constructing an advanced research-scale biomass combustion furnace is the first objective of this work. The constructed furnace should allow observation of PM formation in a biomass combustion system. The furnace should allow flexible adjustment of a combustion setup, i.e. air flow rate, fuel-loading capacity, exhaust gas residence time, and the ratio between primary and secondary air. The furnace should also provide accurate, flexible, and real-time measurement of some important combustion parameters, i.e. temperature, exhaust gas composition, and PM characteristics (composition, morphology, and size distribution).

The development of a biomass particle model is the second objective of this thesis. The model should provide accurate prediction of particle combustion behavior and, consequently, precisely predict PM precursor release. The particle model should also be stable for different particle properties and combustion conditions. The developed model must be sufficient to allow further implementation in a larger scale simulation and CFD analysis framework.

1.3. Outline

This thesis is presented as follows :

Chapter 2 is dedicated to a discussion of biomass thermal decomposition stages with a special highlight on the correlation of these stages with PM precursor release. A discussion of common modelling approaches for different biomass decomposition stages is also presented in this chapter.

Chapter 3 presents the construction of particle mathematical modelling, which includes heat balance, mass balance, and the Stefan flow effect on heat and mass balance.

Chapter 4 describes the simulation setup that was used to simulate the particle model. The discretization method employed in the current work is discussed in this section together with the CFD analysis strategy of heat and mass transfer improvement due to Stefan flow.

Chapter 5 discusses the development of the experimental furnace and its procedures. Some descriptions of measurement techniques are provided in this chapter.

Chapter 6 is dedicated to the presentation and discussion of the main findings. Particle model assessment and validation is described further in this section. Some results showing the stability of the current experimental furnace are also presented.

Chapter 7 summarizes the main findings of this work and presents a proposal for future research.

2. FORMATION OF PARTICULATE MATTER IN A BIOMASS COMBUSTION SYSTEM

2.1. Particle pyrolysis and combustion mechanism

2.1.1. Drying

Water is present as bound water, free water, and water vapor inside a biomass matrix. Water is first taken up as bound water until all available adsorption sites are occupied, and then it becomes free water that fills the biomass pores [18]. Free and bound water may move inside a particle due to capillary forces and diffusion caused by the concentration gradient. Notably, free and bound water have different characteristics with respect to transport and evaporation, which implies that these two different forms of water must be treated carefully [19].

The drying process is modelled from three different approaches in the literature, i.e. equilibrium, heat sink (thermal drying), and Arrhenius (kinetic rate) models [20,21]. The equilibrium model is useful for predicting low-temperature drying conditions, e.g. drying wood for building materials. The heat sink (thermal drying) model relies on step-function evaporation, which can lead to numerical instabilities. The kinetic rate model is used in the present study due to its wide range of temperature applications and high numerical stability, both of which increase simulation robustness and accuracy for fast drying conditions [22].

2.1.2. Devolatilization

Pyrolysis and devolatilization are used interchangeably and refer to the thermochemical degradation process of biomass in the absence of an oxidizer [19]. The different release stages of pyrolytic volatiles divide the devolatilization process into primary and secondary devolatilization where various parallel and consecutive reactions occur. Biomass decomposes into volatile gas, primary tars, and char during primary devolatilization. Secondary devolatilization occurs during the outward transport of primary tars. During this period, primary tars participate in various complex reactions such as cracking, reforming, dehydration, condensation, polymerization, oxidation, and gasification [23]. Secondary devolatilization can be neglected due to its insignificant effect on the simulation [24] based on the assumption that pyrolytic gas exits the biomass particle immediately after it has been devolatilized [17,25–27].

The Arrhenius kinetic rate model is commonly used in particle modelling to describe the devolatilization process. Different reaction schemes with varying degrees of complexity are found

in the literature. The first and the simplest devolatilization model, referred to as the one-step global model, describes biomass decomposition into volatile gas, char, and tar using a single reaction. The second model, which has been widely used, includes three independent competitive reactions. In second model, the solid material is converted competitively into volatile gas, tar, and char [17,18,28–33]. Alternatively, more complex devolatilization mechanisms may be used, including mechanisms based on the three main pseudo components in the biomass (cellulose, hemicellulose, and lignin), which are converted into volatile gas species, tar, and char. Figure 1 illustrates the differences among these three models.

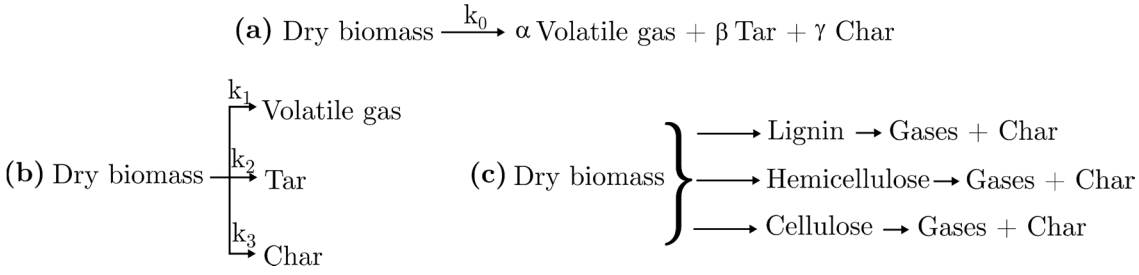

Figure 1. Biomass devolatilization schemes (a) one-step global model (b) three independent competitive reaction models (c) three main pseudo components.

Each devolatilization model has its own advantages and disadvantages and requires the specification of the pre-exponential coefficients and activation energies for the different reactions. In addition, compared with the last two schemes, the implementation of the global model also requires knowledge about the distribution coefficients of each product formed, i.e. α, β and γ. The third model has the advantage of broad prediction of volatile species, which makes the prediction of the composition of pyrolytic gas possibly even more accurate [34,35]. Moreover, it can be applied for various types of biomass in which the composition of the three main pseudo components is known. However, compared with the first and second models, the third model must handle more equations to track the evolution of each pseudo component. Increased computational cost is necessary to utilize the pseudo-component-based model [21]. However, the proposed particle simulation method allows arbitrary schemes to be used.

2.1.3.Char oxidation and gasification

The last stage of biomass particle combustion is heterogeneous char reaction, which involves the reaction of remaining solid carbon (char) with oxidative gases. The char conversion rate is controlled by a series of transport mechanism solid-gas reactions [36] . These include 1) film diffusion of an oxidizing agent, 2) diffusion through the ash layer and particle, 3) adsorption onto the reaction surface, 4) chemical reaction, 5) desorption of product gas from the surface, 6) diffusion of product gas through the particle and the ash layer, and 7) film diffusion back into the

ambient gas. Except for the chemical reaction (step number 4), the remaining steps are mass transport. Based on the Thiele modulus (the ratio of the overall reaction rate to diffusion rate) and the effectiveness factor [37], three different regimes of char conversion can be present in a system, depending on if the reaction takes place inside the particle, at the particle surface, or at both locations. The most influential factor determining the reaction location is the balance between mass transfer and reactions rates, which strongly depends on the temperature [37]. Exothermic combustion increases the surface temperature quickly after ignition, and the reaction becomes mass transfer limited during most of the reaction time.

The simplification of char oxidation and gasification reaction as used in the present study follows the reaction scheme below [19].

$$C + O_2 \xrightarrow{k_4} CO_2$$
$$C + CO_2 \xrightarrow{k_5} 2\,CO$$
$$C + H_2O \xrightarrow{k_6} CO + H_2$$

2.2. Formation of particulate matter precursors

Particulate emission from biomass combustion includes different particle sizes and chemical compositions. Based on size distribution, the particulate matter is typically divided into two different modes, i.e. fine mode (<1 μm) and coarse mode (> 1 μm) [38]. Based on chemical composition, particulate matter emission consists of three main particle components; soot (elemental carbon agglomerates), organic spherical carbon particles, and inorganic ash particles [39].

In brief, inorganic ash particles are formed from inorganic elements that vaporize during combustion. These inorganic vapors nucleate later when the flue gas cools to form ultra-fine particles and may grow by coagulation and condensation. Both organic materials and soot particles are formed due to incomplete combustion. The organic materials in particulate matter are formed by unburnt condensed organic vapor that is originally produced at the devolatilization stage [38]. Condensation might occur in the cooler area, for example, at the chimney. In contrast to organic material, soot particles are formed inside the fuel-rich area of the flame via complex mechanisms. These mechanisms include the formation of soot nuclei from gaseous hydrocarbons which is followed by particle growth due to surface reactions, coagulation, and agglomeration [40]. In optimal combustion conditions, a soot particle can be oxidized in the oxygen-rich area of the flame. A conceptual figure for the formation of the particulate matter contributed from these three components is presented in Figure 2 based on Sippula et al. [13].

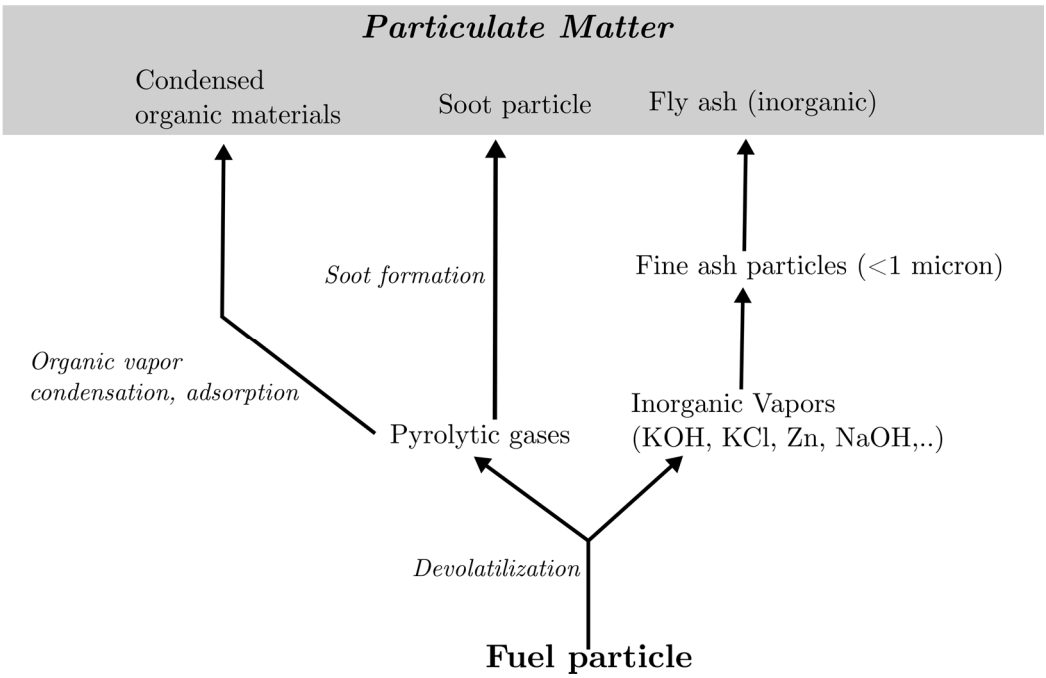

Figure 2. PM formation in biomass combustion [13].

The main precursors of particulate matter are mainly produced during devolatilization. In general, the main precursors of particulate matter are tar, volatile gas, and ash. These precursors can be further converted and grow into solid particulate matter, which really depends on the interaction of the precursors with other components. The precursors conversion into PM also depends on the surrounding conditions at the combustion furnace or stove, i.e. temperature, presence of oxygen and exhaust gas residence time. Therefore, the combination of the accurate prediction of PM precursors and the surrounding conditions in a combustion system are the main requirement to accurately predict PM formation. The accurate prediction of PM formation can be utilized further to reduce the PM emission level in a combustion system in a more efficient way by using modelling and simulation framework.

3. BIOMASS PARTICLE MODELLING

The particle model is formulated by considering the ability of the model to handle important physicochemical phenomena in biomass pyrolysis and combustion, i.e. arbitrary reaction kinetics, local varying properties, heat adsorption by evaporated gas, gradient-driven transport mechanisms such as water movement by diffusion inside biomass matrix, and the inclusion of the effect of Stefan flow on the heat and mass transfer rates at the particle surface. The 1D transient heat and mass balance is constructed as described in the next sub-section.

3.1. Heat balance

The global energy conservation equation for 1D transient simulation follows Eq. (1).

$$\sum \rho_k Cp_k \frac{\partial T}{\partial t} = \frac{1}{r^a}\frac{\partial}{\partial r}\left(r^a \lambda_{eff}\right)\frac{\partial T}{\partial r} - \dot{r}_{v,g}\, Cp_g \frac{V_p}{A_p}\frac{\partial T}{\partial r} + \left(D_{fw} Cp_{fw}\frac{d\rho_{fw}}{dr} + D_{bw} Cp_{bw}\frac{d\rho_{bw}}{dr}\right)\frac{dT}{dr} - \Delta H_{dry}\dot{r}_{v,dry} - \Delta H_{dev}\dot{r}_{v,dev} \quad (1)$$

Where a depends on biomass geometry (0 for planar, 1 for cylinder, and 2 for sphere). The term on the left side of Eq.(1) shows the accumulation term. The boundary condition equation for heat balance at the particle surface follows Eq.(2). Heat conduction into the particle is balanced with heat transfer from or to the particle surroundings by convection and radiation, and heat from the char reaction at the particle surface.

$$\lambda_{eff}\frac{\partial T}{\partial r} = h_{eff}\left(T_{bulk} - T_{surf}\right) - \sigma\omega\left({T_{surf}}^4 - {T_{wall}}^4\right) - \Delta H_{char}\dot{r}_{s,char} \quad (2)$$

3.2. Mass balance

Eqs.(3) to (6) describe the mass evolution of dry wood, free water, char, and bound water. The density adjustment due to particle shrinking and swelling is considered in the last term on the right side in each density evolution equation. The density gradient of free and bound water drives the water movement via diffusion, and this physical phenomenon is accounted for in the first term on the right-hand side of Eqs.(4),(5) and (6).

$$\frac{\partial \rho_b}{\partial t} = -\dot{r}_{v,dev} - \frac{\rho_b}{V}\frac{dV}{dt} \quad (3)$$

$$\frac{\partial \rho_{fw}}{\partial t} = \frac{1}{r^a}\frac{\partial}{\partial r}\left(r^a D_{fw}\right)\frac{\partial \rho_{fw}}{\partial r} - k_4\, \rho_{fw} - \frac{\rho_{fw}}{V}\frac{dV}{dt} \quad (4)$$

$$\frac{\partial \rho_c}{\partial t} = k_3\, \rho_b - \frac{\rho_c}{V}\frac{dV}{dt} \quad (5)$$

$$\frac{\partial \rho_{bw}}{\partial t} = \frac{1}{r^a}\frac{\partial}{\partial r}\left(r^a D_{bw}\right)\frac{\partial \rho_{bw}}{\partial r} - k_5\, \rho_{bw} - \frac{\rho_{bw}}{V}\frac{dV}{dt} \quad (6)$$

The porosity evolution inside biomass is expressed in Eq.(7).

$$\frac{\partial \varepsilon}{\partial t} = -\left(\frac{\partial \rho_b}{\partial t} + \frac{\partial \rho_c}{\partial t} + \frac{\partial \rho_{fw}}{\partial t} + \frac{\partial \rho_{bw}}{\partial t}\right) \times \frac{(1-\varepsilon)}{\rho_{tot}} + \frac{(1-\varepsilon)}{V}\frac{dV}{dt} \tag{7}$$

Volume evolution due to shrinking and swelling during drying, pyrolysis, and char gasification and oxidation is expressed in Eq.(8).

$$\frac{dV}{dt} = \frac{V_0(\beta_m - 1)}{\rho_{fw_0} + \rho_{bw_0}}\dot{r}_{v,dry} + \frac{V_0(\beta_b - 1)}{\rho_{b_0}}\dot{r}_{v,dev} + \frac{A_p \dot{r}_{s,char}}{\rho_{tot}} \tag{8}$$

β_m and β_b are the swelling or shrinking factors for drying and devolatilization. Additional supporting equations for heat and mass balance are listed in Table 1**.** The nominal Nusselt and Sherwood numbers should be corrected due to the effect of Stefan flow, which is discussed in more detail in Section 3.3. The nominal Nusselt and Sherwood numbers before the correction for Stefan flow are summarized in Table 2 for different particle geometries.

Several assumptions are made in the present simulations :

1) Gas behaves as ideal gas.
2) Secondary devolatilization is neglected.
3) Solid biomass is in thermal equilibrium with evaporated gas while it transported out.
4) Particle shrinking only occurs at the char reaction stage. The exclusion of particle shrinking and swelling during drying and pyrolysis is due to the lack of evidence of particle volume evolution during drying and devolatilization in the validation with current experimental data [19].
5) Char oxidation and gasification only occur at the particle surface.
6) High permeability of the ash layer is due to the high amount of Stefan flow.
7) Heat capacity of gas in the accumulation term is neglected due to the insignificant density of gas compared to a solid.

Table 1. Supporting equations for main heat and mass balance

Thermal conductivity	$\lambda_{eff} = \frac{\varepsilon\sigma T^3 d_{pore}}{\omega} + \varepsilon\lambda_g + (1-\varepsilon)\big(\big(x_b + x_{fw}+x_{bw}\big)\lambda_b + x_c\lambda_c + x_{ash}\lambda_{ash}\big)$	(9)
Bound water diffusivity	$D_{bw} = 1.05 \times 10^{-5} \exp\left(\frac{-4633 + 3523\ \frac{\rho_{bw}}{\rho_{tot}}}{T}\right)$	(10)
Devolatilization rate	$\dot{r}_{v,dev} = (k_1 + k_2 + k_3)\ \rho_b$	(11)
Drying rate	$\dot{r}_{v,dry} = k_4\ \rho_{fw} + k_5\ \rho_{bw}$	(12)
Char oxidation rate	$\dot{r}_{s,char} = (k_{6,eff} \times C_{O_2} + k_{7,eff} \times C_{CO_2} + k_{8,eff} \times C_{H_2O}) \times M_c$	(13)
Effective char reaction rate constant (for reaction indexes 4-6)	$k_{i,eff} = \frac{k_i\ h_{m\_eff,i}}{k_i + h_{m\_eff,i}}$	(14)
Kinetic rate constant	$k_i = A_i \exp\left(\frac{-E_{a,i}}{R_g\ T}\right)$	(15)
Gas production rate	$\dot{r}_{v,g} = \dot{r}_{v,dry} + (k_1 + k_2)\ \rho_b$	(16)
Convective mass transfer coefficient	$h_{m,i} = \frac{D_g\ Sh_{eff}}{D_p}$	(17)
Effective convective mass transfer coefficient	$h_{m\_eff,i} = \frac{h_{m,i}\ D_g\ \varepsilon_{ash}}{l_{ash}\left(h_{m,i} + \frac{D_g}{l_{ash}}\right)}$	(18)
Ash layer thickness	$l_{ash} = \frac{\rho_{ash_0}}{\rho_{tot_0}} \times \frac{1}{a+1} \times \left(\frac{r_0^{a+1} - r^{a+1}}{r_0^a - r^a}\right)$	(19)
Effective convective heat transfer coefficient	$h_{eff} = \frac{Nu_{eff}\ \lambda_g}{D_p}$	(20)

Table 2. Nominal Sherwood and Nusselt number equations for different particle geometries

Spherical[34,41]	$Nu = 2 + 0.6\ Re^{0.5} Pr^{1/3}$	(21)	$Sh = 2 + 0.6\ Re^{0.5} Sc^{1/3}$	(22)
Cylindrical[42]	$Nu = (0.4Re^{0.5} + 0.6\ Re^{2/3}) Pr^{0.4}$	(23)	$Sh = (0.4Re^{0.5} + 0.6\ Re^{2/3}) Sc^{0.4}$	(24)
Planar[19]	$Nu = 0.644\ Re^{0.5} Pr^{0.343}$	(25)	$Sh = 0.644\ Re^{0.5} Sc^{0.343}$	(26)

3.3. Effect of Stefan flow on heat and mass transfer

In an effort to improve heat and mass transfer in particle combustion and pyrolysis, it was found that heat and mass exchange at the particle surface should be treated carefully due to the effect of Stefan flow. The general correlation of Sherwood and Nusselt numbers, which are used to determine the rate of mass and heat exchange from or to a particle surface, was calculated based on the flux that originated exclusively from surrounding convective gas flow. In particle combustion and pyrolysis, there is a convective outflow from particle drying and devolatilization that can influence the diffusional transport and the penetration of convective flow from the surrounding gas to the particle surface. Therefore, instead of only considering the flow from the surrounding gas, the net flow between Stefan flow and the surrounding gas flow should be utilized to evaluate a more correct heat and mass exchange from or to the particle surface.

Stefan flow may produce two effects, i.e. enhance or decrease transport in the film around the particle and change the thickness of the "stagnant" film around the particle. In the present modeling, the correction of Sherwood and Nusselt numbers was evaluated by considering Stefan flow into the net flow of gas convective transport in the film layer around the particle and estimating the location of film thickness based on where the concentration or temperature was set to be equal to bulk concentration or temperature.

The calculation is based on the total flux at the surface, which is contributed by the diffusional and convective flux as presented in Eq.(27).

$$N = D\left.\frac{dC}{dr}\right|_{r=R} + u_s C_s = k_c(C_{bl} - C_s) + u_s C_s \tag{27}$$

An analytical solution of Eq.(27) was presented by Bird et.al [43] for a flat surface and by Spalding [44] for $Sh = 2$. A model for diffusion and convection with Stefan flow in the film layer follows:

$$D\left(\frac{1}{r^\alpha}\frac{d}{dr}r^\alpha\frac{dC}{dr}\right) - u\frac{dC}{dr} = 0 \tag{28}$$

The convective flow velocity is dependent on geometry, but it can be written as a function of the velocity at the surface and radius as presented in Eq.(29).

$$u = \frac{u_s R^a}{r^a} \tag{29}$$

In the dimensionless form, Eq.(28) can be transformed into Eq.(30) with $x = r/R$

$$\frac{1}{x^\alpha}\frac{d}{dx}x^\alpha\frac{dC}{dx} - \frac{u_s R}{D}\frac{1}{x^a}\frac{dC}{dx} = 0 \tag{30}$$

Cancelling $\frac{1}{x^a}$ in Eq.(30) produces :

$$\frac{d}{dx}x^{\alpha}\frac{dC}{dx}-\frac{u_s R}{D}\frac{dC}{dx}=0 \tag{31}$$

The integration of Eq.(31) produces :

$$x^{\alpha}\frac{dC}{dx}-\frac{u_s R}{D}\,C=const_1 \tag{32}$$

The solution of Eq.(32) is only a function of the dimensionless number $\frac{u_s R}{D}$, which hereinafter will be called the Andersson number (An), and boundary conditions. Eq.(32) is next solved for spherical geometry with $\alpha=2$, by providing two boundary conditions, one at the surface and one at the boundary layer of the film layer as follows :

BC 1 : $x=1$ and $C=C_s$

BC 2 : $x=x_{bl}=\frac{1}{1-\frac{2}{Sh}}$ (for sphere) and $C=C_{bl}$

Substituting BC 1 to Eq.(32) produces the evaluation of $const_1$ as follows :

$$const_1=-An\,C_s+\left.\frac{dC}{dx}\right|_{x=1}=-An\,C_s+const_2 \tag{33}$$

Substituting Eq.(33) to Eq.(32) and rearranging it produces :

$$\int_{C=C_s}^{C=C(x)}\frac{dC}{C-C_s+\frac{const_2}{An}}=\int_{x=1}^{x=x}An\frac{1}{x^2}dx \tag{34}$$

Solving Eq.(34) produces :

$$\ln\left(\frac{C(x)-C_s+\frac{const_2}{An}}{\frac{const_2}{An}}\right)=An\left(1-\frac{1}{x}\right) \tag{35}$$

Rearranging Eq.(35) becomes as follows :

$$C(x)=C_s+\frac{const_2}{An}\left(e^{\left(1-\frac{1}{x}\right)}-1\right) \tag{36}$$

Inserting the second boundary layer to evaluate $const_2$ in Eq.(36) produces :

$$const_2=An\frac{C_{bl}-C_s}{e^{An\left(1-\frac{1}{x_b}\right)}-1} \tag{37}$$

Substituting Eq.(37) and $\left(1-\frac{1}{x_{bl}}\right)=\frac{2}{Sh}$ based on BC 2, into Eq.(36) produces the final solution of concentration profile in the film layer as presented in Eq.(38) :

$$C(x)=C_s+\frac{C_{bl}-C_s}{e^{2An/Sh}-1}\left(e^{An\left(1-\frac{1}{x}\right)}-1\right) \tag{38}$$

Based on the diffusional transport of gas at the surface in Eq.(27), the corrected Sherwood number can be derived as follows :

$$D\frac{dC}{dr}\Big|_{r=R} = \frac{D}{R}\frac{dC}{dx}\Big|_{x=1} = k_c(C_{bl} - C_s) \tag{39}$$

$$\frac{An}{e^{\frac{2An}{Sh}} - 1}(C_{bl} - C_s) = \frac{Sh_{eff}}{2}(C_{bl} - C_s) \tag{40}$$

$$Sh_{eff} = \frac{2.An}{e^{\frac{2An}{Sh}} - 1} \tag{41}$$

This model assumes no change in film thickness due to Stefan flow. The same analogous derivation is used for the Nusselt number correction, i.e. the heat transfer correction due to Stefan flow as presented below :

For a sphere : $$Nu_{eff} = \frac{2.An_H}{e^{\frac{2An_H}{Nu_0}} - 1} \tag{42}$$

where : $$An_H = \frac{u_s \rho Cp R}{\lambda_g} \tag{43}$$

An_H is equal to An if the Lewis number is 1. A simple adjustment to the model is performed by recalculate a new Reynolds number that takes Stefan flow into account as shown in Eq.(44). Re_{adj} is used to calculate nominal Sherwood number in Table 2.

$$Re_{p,adj} = (u_{bulk} - u_s)d/\nu \tag{44}$$

The degree of accuracy and range of applicability of the current analytical solution was tested further by a comparison with CFD simulations. The current analytical solution was also compared with classical Sherwood number correction correlations due to Stefan flow. Some of the classical models that are compared in the present work are the Spalding [44] and Michaelides [45] models.

$$Sh_{eff,spalding} = \frac{\ln(1 + B_M)}{B_M} Sh \tag{45}$$

$$Sh_{eff,michaelides} = \frac{2 + 0.87\, Re^{\frac{1}{2}} Sc^{\frac{1}{3}}}{(1 + B_M)^{0.7}} \tag{46}$$

$$\text{where } B_M = e^{An/2} - 1 \tag{47}$$

4. SIMULATION STRATEGY

4.1. 1-Dimensional particle simulation

A common basic assumption for single particle modelling, which depends on whether temperature non-uniformity can be neglected or not, decides the level of mathematical modelling complexity. The uniformity of particle temperature is evaluated with a dimensionless number, the Biot number (Bi), which distinguishes particles as thermally thin, $Bi < 0.1$, and thermally thick, $Bi > 0.1$ [17].

$$Bi = \frac{h_{eff}\, d}{\lambda} \tag{48}$$

A thermally thin particle assumes that the temperature non-uniformity throughout the particle can be ignored, however, it cannot be ignored in a thermally thick particle. In consequence of that, different biomass decomposition stages, i.e. drying, devolatilization, and combustion, can occur simultaneously over a thermally thick particle. A modelling approach that allows spatial and time resolution is needed to model a thermally thick particle, and such an approach escalates modelling complexity.

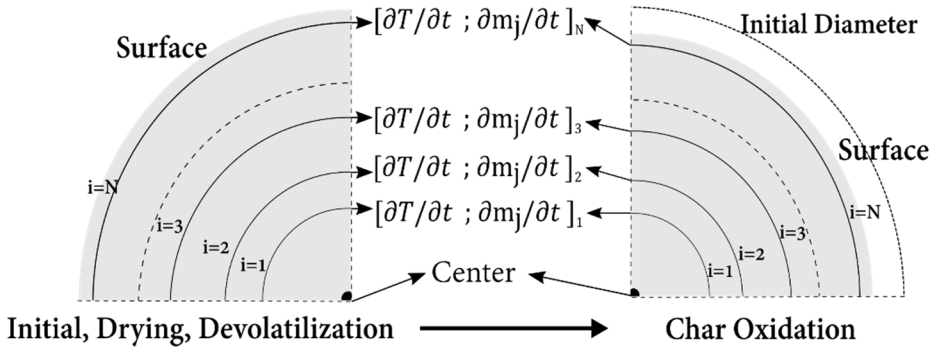

Figure 3. Mesh-based particle discretization scheme

As presented in **Paper I**, in order to simulate thermally thick particle combustion, two different particle discretization approaches have been used by researchers, i.e. mesh-based discretization [19,22,28,31,32,41,46,47] and interface-based discretization [16,17,25–27,29,34,48]. Mesh-based discretization relies on numerical discretization, which divides each particle into several grid points and directly solves all governing equations at each grid point, as described in Figure 3 [21]. In contrast to the mesh-based model, the interface-based model relies on physical discretization, which divides the particle into layers based on available biomass component mass, as described in Figure 4. The layers in the interface-based model can be composed of either dry wood, moisture, char, or ash [27].

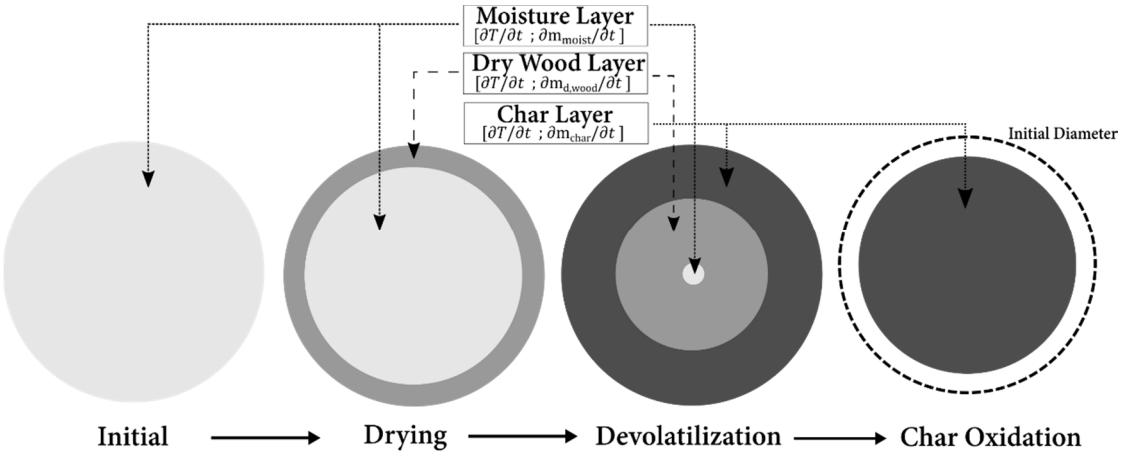

Figure 4. Interface-based particle discretization scheme

Both aforementioned discretization methods have their own advantages and disadvantages in terms of numerical efficiency and accuracy. Briefly, the mesh-based model allows higher accuracy than the interface-based model. This is due to mesh-based model uses more computational grids than interface-based model. However, this computational accuracy comes with a price, which is higher computational power than the interface-based model. In contrast, the efficiency of the interface-based model is confirmed by its applicability in larger scale simulation works, i.e. multi particle modelling and biomass furnace simulation.

Table 3. Conceptual summary of different discretization models with regard to ability to include physical phenomena in mathematical modelling

Physical phenomena	Mesh	Interface	Collocation
Decoupling between species and space resolution	++	-	++
Smooth species profile	++	-	+
Water transport inside particle due to diffusion	++	-	++
Distinction of bound and free water	++	*	++
Heat exchange between solid and evaporated gas	++	++	++
Consecutive gas reaction occurs inside particle, i.e. secondary devolatilization	++	-	++
Stefan flow effect	*	*	++
Particle shrinking and swelling during drying, devolatilization, and char reaction	++	++	++
Easy implementation as sub-grid models for CFD analysis (multi particle and furnace)	-	++	+

(++) high degree of agreement ; (+) good agreement ; (-) disagreement ; *possible to be implemented

4.1.1.Particle discretization using orthogonal collocation

Based on the remaining challenges to simulate a thermally thick particle, another approach of particle discretization was employed, i.e. the orthogonal collocation method. The main reason for the selection of the orthogonal collocation method for particle discretization was its ability to transform PDEs into the ODE form. This transformation allows the current model to be implemented in the CFD environment. Moreover, orthogonal collocation has been found to work well with various problems such as mass and heat diffusion and reaction [49–57]. An overview of the orthogonal collocation method compared to the interface- and mesh-based models in terms of ability to handle specific physical phenomena is shown in Table 3.

The orthogonal collocation method discretizes the biomass particle into several collocation points and solves the governing equations at each collocation point. The discretization scheme looks similar to numerical discretization, which is used in the mesh-based model. However, the mesh-based model usually uses a backward, forward, or center scheme to solve ODE, which only utilizes the adjacent grid points to calculate an observed point. The orthogonal collocation method utilizes values from all numerical grids, or collocation points, to calculate the value at an observed cell. This leads to a significant reduction of numerical grids employed, and the result is few grids to achieve mesh independence. This will be presented in Section 6.1.1.1., in comparison with many more numerical grids that are typically needed by the ordinary mesh-based model.[22,58,59]

Table 4. The location of collocation points for different geometries (planar, cylindrical, and spherical)

N	Geometry		
	Planar	Cylindrical	Spherical
1	0.57735 02692	0.70710 67812	0.77459 66692
2	0.33998 10436	0.45970 08434	0.53846 93101
	0.86113 63116	0.88807 38340	0.90617 93459
3	0.23861 91861	0.33571 06870	0.40584 51514
	0.66120 93865	0.70710 67812	0.74153 11856
	0.93246 95142	0.94196 51451	0.94910 79123
4	0.18343 46425	0.26349 92300	0.32425 34234
	0.52553 24099	0.57446 45143	0.61337 14327
	0.79666 64774	0.81852 94874	0.83603 11073
	0.96028 98565	0.96465 96062	0.96816 02395
5	0.14887 43390	0.21658 73427	0.26954 31560
	0.43339 53941	0.48038 04169	0.51909 61292
	0.67940 95683	0.70710 67812	0.73015 20056
	0.86506 33667	0.87706 02346	0.88706 25998
	0.97390 65285	0.97626 32447	0.97822 86581

In the orthogonal collocation method, the solution of differential equations is approximated using orthogonal polynomials. There are several orthogonal polynomial trial functions that can be utilized with different orders of x and one of the most common functions called shifted Legendre orthogonal polynomials, which is constructed as a function of x^2. The expanded solution for temperature at a collocation point using shifted Legendre orthogonal polynomials is described in Eq.(49) with N as the total collocation points.

$$T(x_j) = \sum_{i=1}^{N+1} d_i x_j^{2i-2} \tag{49}$$

The shifted Legendre orthogonal polynomial is defined in Eq.(50) with a =1, 2, or 3 for planar, cylindrical, or spherical geometry, respectively.

$$\int_0^1 W(x^2) P_k(x^2) P_m(x^2) x^{a-1} dx = 0 \qquad k \leq m-1 \tag{50}$$

The roots of shifted Legendre polynomials provide the coordinates of the collocation points as listed in Table 4. The first and second derivatives of Eq.(49) follow the forms that are presented in Eq.(51) and (52).

$$\frac{dT}{dx}(x_j) = \sum_{i=1}^{N+1} d_i (2i-2)\, x_j^{2i-3} \tag{51}$$

$$\frac{d^2T}{dx^2}(x_j) = \sum_{i=1}^{N+1} d_i (2i-3)(2i-2) x_j^{2i-4} \tag{52}$$

In the matrix form, the expanded solution for all collocation points in Eq.(49) from the first point (i =1) to the last point (i =$N+1$) follows :

$$\begin{bmatrix} T_1 \\ T_2 \\ T_3 \\ \vdots \\ T_{N+1} \end{bmatrix} = \begin{bmatrix} 1 & x_1^2 & x_1^4 & \cdots & x_1^{2N} \\ 1 & x_2^2 & x_2^4 & \ldots & x_2^{2N} \\ 1 & x_3^2 & x_3^4 & \ldots & x_3^{2N} \\ \vdots & \vdots & \vdots & \ddots & \vdots \\ 1 & x_{N+1}^2 & x_{N+1}^4 & \ldots & x_{N+1}^{2N} \end{bmatrix} \begin{bmatrix} d_1 \\ d_2 \\ d_3 \\ \vdots \\ d_{N+1} \end{bmatrix} \tag{53}$$

$$\text{or} \quad \boldsymbol{T} = \boldsymbol{Q}\boldsymbol{d} \tag{54}$$

In order to solve the remaining unknowns in Eq.(54), which are $\boldsymbol{T}$ and $\boldsymbol{d}$, the substitution from the solution for all collocation points to the solution for each collocation point was performed with $\boldsymbol{d}$ matrix substitution.

$$\boldsymbol{d} = \boldsymbol{Q}^{-1}\boldsymbol{T} \tag{55}$$

$$T(x_j) = \left(\sum_{i=1}^{N+1} x_j^{2i-2}\right)\boldsymbol{Q}^{-1}\boldsymbol{T} \tag{56}$$

The last form of the temperature expansion solution in Eq.(56) can be solved, since the remaining unknown is equal to the total number of equations. The remaining unknowns are contributed from $N+1$ number of $T(x_j)$. The $N+1$ equations are consisted of the N number of Eq.(56) at each collocation point and one equation from the surface boundary condition equation. The choice of trial function, Eq.(49), automatically ensures the symmetry boundary condition in that the center of the particle is fulfilled at each instance in time.

The same scheme can be used for the first and second derivatives of temperature, which are described as:

$$\frac{\boldsymbol{dT}}{\boldsymbol{dx}} = \boldsymbol{Cd} \longrightarrow C_{ji} = (2i-2)x_j^{2i-3} \longrightarrow \frac{dT}{dx}(x_j) = \left(\sum_{i=1}^{N+1} C_{ji}\right)\boldsymbol{Q}^{-1}\boldsymbol{T} \rightarrow \frac{dT}{dx}(x_j) = \boldsymbol{AT} \tag{57}$$

$$\frac{\boldsymbol{d^2T}}{\boldsymbol{dx^2}} = \boldsymbol{Dd} \rightarrow D_{ji} = (2i-3)(2i-2)x_j^{2i-4} \rightarrow \frac{d^2T}{dx^2}(x_j) = \left(\sum_{i=1}^{N+1} D_{ji}\right)\boldsymbol{Q}^{-1}T \rightarrow \frac{d^2T}{dx^2}(x_j) = \boldsymbol{BT} \tag{58}$$

At this stage, the first and second derivatives of the temperature substitution with orthogonal collocation coefficients ($\boldsymbol{A}$ and $\boldsymbol{B}$) in Eqs.(57) and (58) can be used to solve the global heat balance in Eq.(1). The orthogonal collocation method requires that the space variable is transformed into the dimensionless form, in range of 0 for center and 1 for the surface, as presented below:

$$r = xR \qquad \frac{\partial T}{\partial r} = \frac{1}{R}\frac{\partial T}{\partial x} \qquad \frac{d^2T}{dr^2} = \frac{1}{R^2}\frac{d^2T}{dx^2}$$

The final form of PDE heat balance at a collocation point in Eq.(1) is transformed into ODE heat balance in Eq.(59).

$$\begin{aligned}\sum \rho_{k,j} Cp_{k,j}\frac{\partial T}{\partial t} = {} & \frac{\lambda_{eff,j}}{x^a R^2}\left(ax\left(\sum_{i=1}^{N+1} A_{j,i}T_i\right) + x^a\left(\sum_{i=1}^{N+1} B_{j,i}T_i\right)\right) \\ & - \dot{r}_{v,gas,j}\, Cp_{g,j}\frac{V_p}{RA_p}\left(\sum_{i=1}^{N+1} A_{j,i}T_i\right) \\ & + \left(D_{fw,j}Cp_{fw,j}\left(\sum_{i=1}^{N+1} A_{j,i}\rho_{fw_i}\right) + D_{bw,j}Cp_{bw,j}\left(\sum_{i=1}^{N+1} A_{j,i}\rho_{bw_i}\right)\right)\sum_{i=1}^{N+1} A_{j,i}T_i \\ & - \Delta H_{dry,j}\dot{r}_{v,dry,j} - \Delta H_{dev,j}\dot{r}_{v,dev,j}\end{aligned} \tag{59}$$

Another set of equations transformed into the orthogonal collocation format, i.e. boundary condition and component balance, must follow the transformation of heat balance in Eq.(59) by substituting the space notation into the dimensionless one and replacing the derivative term with the orthogonal collocation coefficients.

4.1.2.Moving coordinates

Temperature interpretation based on the heat balance in Eq.(1) must be revised due to the transformation of the space variable into the dimensionless form using the orthogonal collocation method. The revision of the accumulation term is needed during particle shrinking since the space variable is bounded between 0 and 1, even when the physical dimension changes in time due to char reaction, i.e. particle radius, $R = f(t)$. The updated temperature reading follows Eq.(60)

$$T_{new} = T_{old} + \frac{1}{R}\frac{\partial T}{\partial x}\frac{\partial R}{\partial t}dt \tag{60}$$

In the first derivative form, Eq.(60) produces :

$$\frac{\partial T_{new}}{\partial t} = \frac{\partial T_{old}}{\partial t} + \frac{1}{R}\frac{dT}{dx}\frac{dR}{dt} \tag{61}$$

Eq.(61) can be substituted into the accumulation term in Eq.(1) to produce a revision of the accumulation term, as presented in Eq.(62). Eq.(62) can be transformed into discretized form by orthogonal collocation, as presented in Eq. (63).

$$\sum \rho_k Cp_k \left(\frac{\partial T}{\partial t} + \frac{1}{R}\frac{\partial T}{\partial x}\frac{\partial R}{\partial t}\right) \tag{62}$$

$$\sum \rho_k Cp_k \left(\frac{\partial T}{\partial t} + \frac{1}{R}\left(\sum_{j=1}^{N} A_{i,j}T_j\right)\frac{\partial R}{\partial t}\right) \tag{63}$$

4.1.3.Source term evaluation

Biomass decomposition inside a particle is a continuous process that moves from the particle surface toward the particle center at a rate determined by heat wave propagation. The reaction rate using the orthogonal collocation method was calculated only at specific collocation points. The utilization of a kinetic rate with a very high activation energy or narrow reaction zone produced an unsmooth transition of mass reduction since the temperature was not sufficient to start the reaction in the inner collocation points while the reaction was completed at the outer collocation point. This less smooth transition might produce a fluctuation of mass loss in a global calculation and uneven

release of pyrolytic gases and water vapor. This uneven release of pyrolytic gases and water vapor might cause challenges to obtain convergence CFD simulations.

The utilization of more collocation points is expected to reduce this problem, but a result of this action is that higher computational efforts are also needed. Another alternative method without adding more collocation points is to expand the coverage of the reaction rate at one specific collocation point, which was performed in the current research. The idea behind the improvement was to evaluate the reaction rate in the area between each collocation point and bring the average reaction rate value over the area into the collocation point calculation. The reaction rate was averaged using mass weighting average which follows Eq.(64) (k= reaction and components index, i = collocation points index, j = Euclidean points index and l = expansion points index).

$$\bar{\dot{r}}_{v,k,i} = \frac{\int_{r_{j-1}}^{r_{j+1}} A_{k,l} \exp\left(-\frac{E_{a_k}}{R_g T_l}\right) \times \rho_{k,l} \times A_{layer,l}\, dr}{\int_{r_{j-1}}^{r_{j+1}} \rho_{k,l} \times A_{layer,l}\, dr} \times \rho_i \tag{64}$$

$(j+1)$ and $(j-1)$ are the Euclidean points to the left and the right of a collocation point. The Euclidean point was calculated based on the middle position of adjacent collocation points. $A_{layer,j}$ is the perpendicular area of expansion layer which is equal as, $4\pi r^2$ for spherical, $2\pi r L_p$ for cylindrical and $L_p \times W_p$ for planar. The reaction rate was evaluated over expansion points that were located between two Euclidean points, and the mass weighted average reaction rate was used as the reaction rate at each collocation point.

The value of the reaction rate at the Euclidean points, and any other expansion points outside the collocation points, was calculated based on the interpolated value of temperature and density. Density and temperature value at the expansion points, were calculated from the temperature and density values at the collocation point. Different interpolation methods were employed herein for density and temperature. Temperature values at the expansion points can be calculated using the solution of the expansion form of temperature in Eq.(49), as long as the value of d is available. The value of d can be calculated using Eq.(55) since the value of Q , which is a function of x, and T are available.

The density at the expansion points were interpolated using the piecewise cubic hermite polynomial method. The cubic hermite interpolation has been proven to produce better results than quadratic and linear interpolations in assessing the reaction rate correction in the sub-grid scale [60]. The piecewise cubic hermite polynomial method using a third-order polynomial to calculate the dependent variable at the observed point is described in Eq. (65). The coefficients of the cubic interpolation are derived from the value from adjacent points [61].

$$\rho_k(x) = a(x - x_{i-1})^3 + b(x - x_{i-1})^2 + c(x - x_{i-1}) + d \quad (65)$$

4.2. CFD simulation of Stefan flow effect

The current analytical solution for an effective Sherwood number due to the effect of Stefan flow was validated by comparing the analytical solution results with CFD simulation results using ANSYS Fluent. CFD simulation herein is limited to laminar flow, i.e. bulk Reynolds numbers < 2000 and low particle Reynolds numbers, Re_p, where mass and heat transfer are steady. The particle Reynolds number regions were kept to be below 150 for current spherical particle analysis, in order to maintain a steady Sherwood number and avoid periodic vortex shredding.

A particle was modelled as a thin hollow sphere with the thickness $0.01\, d_p$. A very fast irreversible reaction of $A \rightarrow A^*$ at the particle surface was utilized, which produced a concentration of A on the surface close to zero. Identical properties of A and A^* were utilized to eliminate a net flow caused by the reaction. The source of Stefan flow was a mass source in the thin particle surface which produced the same flow rate in all directions. This setup corresponds to a particle with equal heating rate on the whole surface e.g. by uniform radiation or very high heat conductivity. Simulations were done for a range of Stefan flow.

The computational domain was cubic with a length 20 times larger than the particle radius. This was done to avoid any significant velocity increase around the particle caused by the presence of the wall. The computational domain was meshed into 2.2 million cells with a very fine mesh close to the surface. The mesh independence result was achieved after an adaption that used the gradient of species and pressure and produced about 4.7 million cells. A high quality mesh of prism layers in the surface region were used as depicted in Figure 5 to minimize numerical diffusion. The mesh independence result was achieved after an adaption that used the gradient of species and pressure.

The boundary conditions which were used in the simulation i.e. the inlet flow was set as velocity boundary condition, the outlet condition was set as outflow, a free slip condition at the walls, and no slip condition at the particle surface. The continuity, momentum and species balance were calculated using Eqs.(66), (67)and (68) in ANSYS Fluent software [62].

$$\frac{\partial \rho}{\partial t} + \nabla.(\rho \vec{v}) = S_m \quad (66)$$

$$\frac{\partial}{\partial t}(\rho \vec{v}) + \nabla.(\rho \vec{v}\vec{v}) = -\nabla p + \nabla.(\bar{\bar{\tau}}) + \rho \vec{g} + \vec{F} \quad (67)$$

$$\frac{\partial}{\partial t}(\rho Y_i) + \nabla.(\rho \vec{v} Y_i) = -\nabla.\vec{J_i} + R_i + S_i \quad (68)$$

Those equations were discretized further using second-order accurate schemes, and the pressure-velocity coupling was handled using the SIMPLE algorithm. The governing equations were solved using a segregated solver approach with ANSYS Fluent 19.0.

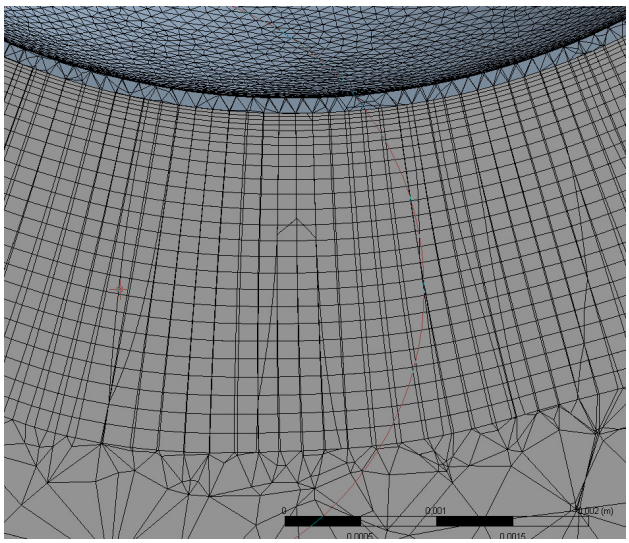

Figure 5. Cross section in the computational mesh.

The formation of A^* was limited by the diffusion of A to the surface. Consequently, the estimation of the Sherwood numbers for transport with Stefan flow can be estimated from net outflow of A, as presented in Eq.(69), or from outflow of A^* at the outlet, as presented in Eq.(70). The third way of determining the Sh number was using the volume integral of the reaction rate in the porous volume, as given by Eq.(71). The Sherwood number evaluation from those three different approaches were compared to ensure the simulation accuracy.

$$Sh_{CFD} = \frac{d_p}{D_A \Delta C_A \, A_p} \left(\int_{A_{inlet}} u_x C_A dA_{inlet} - \int_{A_{outlet}} u_x C_A dA_{outlet} \right) \tag{69}$$

$$Sh_{CFD} = \frac{d_p}{D_{A^*} \Delta C_{A^*}} \left(\frac{\int_{A_{outlet}} u_x C_{A^*} dA_{outlet}}{A_p} - u_s C_{A_s^*} \right) \tag{70}$$

$$Sh_{CFD} = \frac{d_p}{D_A \Delta C_A \, A_p} \int_{V_{porous}} r_A dV \tag{71}$$

5. EXPERIMENTAL WORK

5.1. Grate furnace

In order to obtain more detailed phenomena about biomass combustion behavior and PM formation in biomass combustion, an experimental apparatus was designed and constructed. A fixed-bed furnace, commonly called a grate furnace, was built to allow detailed observation of different combustion parameters and characteristics of particulate matter. A grate furnace has several advantages over other common commercial furnace types. These advantages include lower investment, lower operating cost, lower dust load in the flue gas, and less sensitivity to slagging than fluidized-bed furnaces [63]. The scheme for the constructed grate furnace is shown in Figure 6.

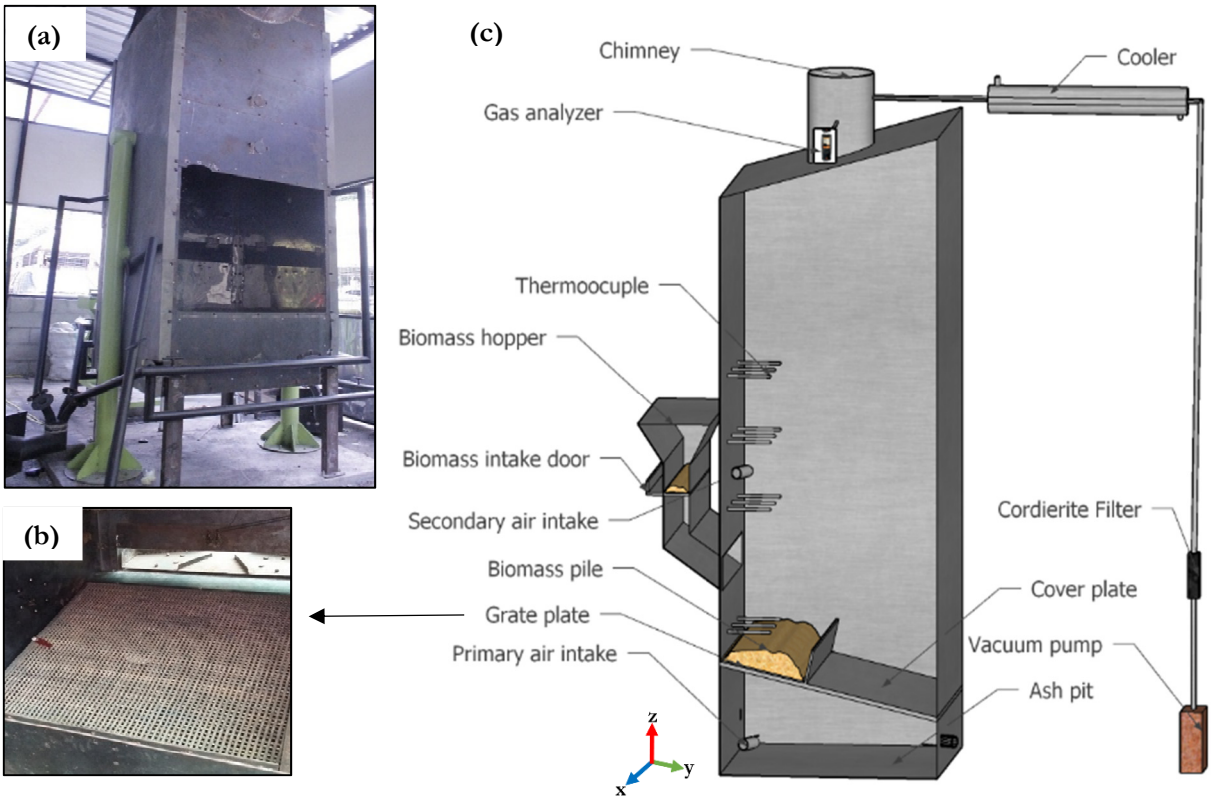

Figure 6. (a) Photograph of grate furnace without heat insulation (b) grate or perforated plate, and (c) schematic figure of grate furnace.

As shown in Figure 6, primary air is introduced from the bottom part of the grate plate, and the air meets solid biomass, which remains above the perforated plate. Secondary air enters above the biomass bed to help combustion proceed in the gas phase. The solid biomass enters into the furnace via a hopper by exploiting gravity to transfer biomass from the hopper to the grate plate.

The exhaust gas flows through the room above the grate, called the freeboard, before it goes to the chimney. The freeboard volume of the current furnace was 3 meters x 1 meter x 1 meter (H x W x L). Several 0.8 mm thermocouples, type K, were placed in the freeboard to measure the temperature evolution of gas. Some of the exhaust gas was sucked into the PM trapping system, while most of it flowed through a 3-meter high chimney before being released to the environment.

In order to support detailed observation of different experimental setup effect on the evolution of combustion parameters and PM characteristics, some flexible features have been prepared in this constructed furnace, i.e.:

- Portable gas analyzer to measure the composition of gas at different places.
- Portable PM trapping system to sample PM particles at different places in the furnace.
- Adjustable grate plate opening to facilitate different capacities for biomass loading.
- Baffles that can quite easily be installed in the freeboard to enhance residence time.
- Adjustable primary and secondary air flowrates.
- Air heater for primary and secondary air.

The constructed furnace was also equipped with proper heat insulation to minimize heat loss from freeboard to environment. Two layers of insulation were attached to furnace wall, i.e. 5 cm of ceramic wool and 20 cm of glass wool. Two different materials were utilized because different temperature levels are expected to be present inside the insulation. Ceramic wool was attached closer to the furnace wall since it has a higher melting temperature about 900°C, and glass wool, which has a lower melting temperature about 400°C, was placed outside the ceramic wool layer.

5.1.1. Air intake mechanism

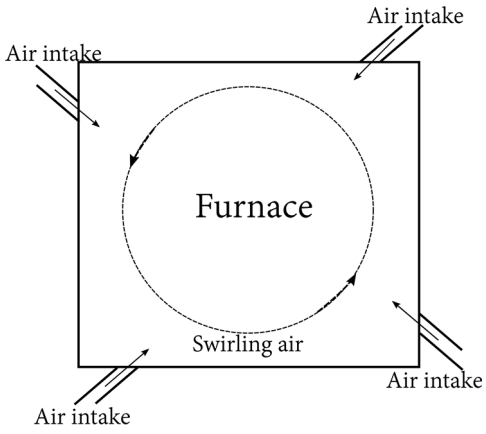

Figure 7. Tangential injection of primary and secondary air schematic figure.

Primary and secondary air to the furnace were supplied by an adjustable blower. The air flow from the blower was divided into four smaller pipes and inserted tangentially from four different

sides of the furnace as shown in Figure *7*. This tangential air injection mechanism was designed to enhance the mixing of air and gas fuel in the freeboard. Tangential air injection produces a strong rotating flow on the horizontal cross sections, which has been proven to produce better fuel burnout. Another advantage of tangential air injection is the deposit formation and corrosion mitigation on the furnace wall that is caused by the breaking of the air curtain close to the furnace walls, which prevents local oxidative conditions [4].

5.1.2.PM trapping system

The PM trapping system consisted of cooler, PM cordierite filter (Figure 8), and vacuum pump. Exhaust gas in the freeboard or chimney was sucked through a sampling pipe and proceeded to temperature cooling using a 2-meter long double pipe heat exchanger with hot gas flows inside the tube and water on the shell side. The high temperature inside the cordierite filter was avoided in order to prevent PM oxidation inside it. PM particles that had been captured in the filter were investigated further to obtain characteristics, i.e. chemical composition, morphology, size distribution, and reactivity.

Figure 8. Particulate matter filter.

5.2. Measurements

5.2.1.Temperature measurement

As presented in Figure 6, several 0.8 mm type K thermocouples were employed to keep track of the temperature evolution inside the freeboard. A type K thermocouple has a maximum measurement limit up to 1100°C. There are three different locations of the thermocouple in the x-axis, i.e. 30 cm (A), 50 cm (B), and 70 cm (C) from the front side (the side where the biomass is introduced). This is presented schematically in Figure 9.

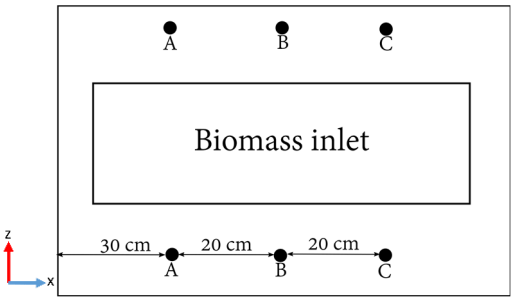

Figure 9. Thermocouple coordinate on the x axis.

There are four different thermocouple positions in the z-axis, i.e. 60 cm, 115 cm, 145 cm, and 175 cm from the ash pit. In total, there are 12 thermocouples, which corresponds to each representative position in the x and z directions. All thermocouples were inserted about 20 cm in the y direction from the biomass inlet side. The wall temperature was also monitored by inserting a thermocouple to 1 mm depth into a 5 mm steel wall. Two thermocouples were placed in the furnace, and these monitored the wall temperature above the biomass inlet position (front side) and on the side that was opposite the biomass inlet (back side). The thermocouples were connected to a Data Taker DT85 Series 3 data logger that captured temperature data every two seconds.

5.2.2. Two-Thermocouple Method

The measurement of the gas temperature in a combustion furnace using thermocouples may significantly differ from the real gas temperature for several reasons. One of the reasons is radiative heating or cooling of the thermocouple bead [64]. A thermocouple bead can measure different gas temperatures due to the transfer of heat transfer via radiation to the surrounding solid, i.e. the furnace wall. This problem can be diminished if the surrounding wall temperature reaches the same temperature level as the gas phase. However, this uniform temperature of gas and solid phases is very hard to achieve since continued heat loss to the environment is inevitable in the current furnace.

In order to obtain a more accurate measurement of gas temperature, the two-thermocouple method was used. The radiation error in this method is encountered when two thermocouples with the same materials but with different sizes are used. More correct gas temperature can be calculated based on the difference of two thermocouple measurements. Gas temperature was calculated using Eq.(73), which derived from the steady state energy balance equation on the thermocouple for smaller and larger thermocouple diameters in Eq.(72). l corresponds to the large diameter thermocouple and s is for the smaller one.

$$h(T_g - T_b) = \varepsilon_b \sigma (T_b^4 - T_\infty^4) \tag{72}$$

$$T_g = \frac{\varepsilon_b \sigma (T_{b,s}^2 - T_{b,l}^2)(T_{b,s} - T_{b,s})(T_{b,s} - T_{b,l})}{h_s - h_l} + \frac{h_s (T_{b,s} - T_{b,l})}{h_s - h_l} + T_{b,l} \tag{73}$$

5.2.3.Exhaust gas composition.

The composition of exhaust gas was recorded with a Testo 320 Portable Gas Analyzer. The analyzer was able to capture O_2 and CO composition with high accuracy, as presented in Table 5.

Table 5. Testo 320 portable gas analyzer technical specification.

Elements	**Measuring range**	**Resolution**	**Response time**	**Accuracy**	**Sensor type**
O_2	0-21% vol	0.1% vol	20 s	±0.2% vol	Electrochemical
CO	0-8000 ppm	1 ppm	60 s	±20 ppm (0 to 400 ppm) ±5% of measured value (401 to 2000 ppm) ±10% of measured value (2001 to 4000 ppm)	Electrochemical

The response time in Table 5 corresponds to the reaction time inside the sensor. The response time information is important to determine the correct real time measurement value for data post-processing and for further validation with the simulation. Both O_2 and CO sensors use the electrochemical method to measure the composition of the targeted component in the exhaust gas. An electrochemical sensor has three major parts: an anode, a cathode, and a pool of electrolyte in between. Oxygen molecules in exhaust gas are reduced at the cathode as follows:

$$4e^- + 2H_2O + O_2 \rightarrow 4\,OH^-$$

The hydroxyl ions that were produced in the cathode migrate through the liquid electrolyte to the anode and simultaneously start the anode reaction as follows :

$$Pb + OH^- \rightarrow PbO + H_2O + 2e^-$$

The net cell reaction is as follows:

$$2\,Pb + O_2 \rightarrow 2\,PbO$$

The migration of hydroxyl ions generates the electric current in the external electrical circuit. This electric current is proportional to oxygen concentration and it is used to monitor oxygen concentration [65].

5.3. Experimental procedures

The biomass used for the experiments was coconut shell, as shown in Figure 10. Coconut shell is considered as a side or waste product of coconut fruit and is 20% of the total mass of coconut. Indonesia is the world leader in coconut production with about 18 million tons produced in 2017 [66], which corresponds to approximately 3.6 million tons of coconut shell.

The abundant resource of the coconut shell has not been utilized in optimum ways today. Whereas, the coconut shell has high potential as renewable energy sources for power generation due to high energy content (about 18 MJ/kg). Very low moisture and ash contents in the coconut shell also can be beneficial in a combustion furnace. This resource can be very promising to be used especially for household rural energy, in the developing countries where they grow [67].

Figure 10. Raw coconut shell.

Coconut shell for the experimental purpose was collected from local suppliers in Yogyakarta, Indonesia, who sell coconut fruit and its water as main products. For experimental purposes, the 5 mm thick coconut shell was crushed to size of 5 cm x 5 cm and dried for a short period of time using solar heat for about 8 hours. This drying period is considered to be sufficient since raw coconut shell has a very lower moisture content. Proximate and ultimate analyses of the coconut shell were conducted, and the results are summarized in Table 6.

Table 6. Ultimate and proximate analysis results (in %mass).

Ultimate Analysis				**Proximate Analysis (wet basis)**			
Carbon	**Hydrogen**	**Oxygen**	**Nitrogen**	**Volatile**	**Ash**	**Fixed Carbon**	**Moisture**
47.5	6.23	45.47	0.11	72.4	0.6	19.4	7.6

Preliminary experiments to test the stability and repeatability of the furnace were conducted. The operating conditions for the experiments are listed below :

- Primary air volumetric flow rate = 38 L/s ; Secondary air volumetric flow rate = 0 L/s
- Grate opening for biomass bed = 25% from total grate area
- Coconut shell loading = 1 kg/3 minutes or 20 kg/hour.

The combustion experiment was conducted in four different stages. The first stage is called the LPG pre-heating. This stage was started by inserting 5 kg of biomass above the grate plate and heating up the combustion chamber using an LPG burner. The pre-heating stopped when the biomass started to ignite by itself after reaching a certain level of temperature.

The next stage after the pre-heating stage is called the transient stage. In this second stage or transient stage, 1 kg of biomass was loaded every three minutes. The temperature evolution from the thermocouple measurement in the freeboard and wall furnace was monitored during this stage until average temperature measurements reached steady stage, or the third stage. The transient stage was expected to take a long time due to the massive amount of thermal mass from the wall furnace, which was heated from cold conditions.

The steady stage was reached when the average temperature evolution from the thermocouple reading displayed a constant value or an insignificant change from one to the next reloading period. In this steady stage, the composition of the exhaust gas composition was measured using a portable gas analyzer. The steady stage was finished when all important combustion parameters had been completed recorded.

The final stage of the combustion experiment was the cooling stage. In this stage, reloading of the biomass was stopped while a supply of cold primary air was maintained. The measurement of the exhaust gas composition in this stage must be recorded. The exhaust gas measurement was stopped when combustion was complete, which was indicated when the gas analyzer showed 21% oxygen.

6. RESULTS AND DISCUSSION

6.1. Particle modelling

MATLAB 2016b ® was used to simulate the resulting system of coupled algebraic-differential equations, specifically the built-in ODE solver (ode15s). For the purpose of validating the accuracy of the orthogonal collocation method, the partial differential equations were solved directly with the built-in PDE solver (pdepe). A numerical accuracy test was performed by comparing the simulation results at conditions relevant to the experimental results performed by other researchers. A list of experiments from Case A to D and corresponding operating conditions is presented in Table 7, which consists of poplar wood pyrolysis and combustion in different geometries and initial moisture contents.

Table 7. Experimental conditions from Lu et al.[19].

Experiment condition	Case A	Case B	Case C	Case D
Wall temperature (K)	1276	1276	1276	1276
Gas temperature (K)	1050	1050	1050	1050
Initial moisture content (wt%)	6	6	40	40
Gas material	Nitrogen	Nitrogen	Nitrogen	Air
Particle shape	Sphere	Cylinder	Cylinder	Sphere
Particle material	Poplar	Poplar	Poplar	Poplar
Particle diameter (mm)	9.5	9.5	9.5	9.5

Table 8. Kinetic rate data.

Index	Reaction	A (s^{-1})	Ea (kJ mol^{-1})	ΔH (kJ kg^{-1})
One step global scheme : [68]				
0	Dry biomass → 0.46 Gas + 0.46 Tar + 0.08 Char	7.41×10^4	83.6	150
Three independent competitive reaction schemes : [19]				
1	Dry biomass → Gas	1.11×10^{11}	177	418
2	Dry biomass → Tar	9.28×10^9	149	418
3	Dry biomass → Char	3.05×10^7	125	418
Char oxidation and gasification : [19]				
4	$C + O_2 \rightarrow CO_2$	$0.658\,T$ (m s^{-1})	74.8	-32000
5	$C + CO_2 \rightarrow 2CO$	$3.42\,T$ (m s^{-1})	130	14370
6	$C + H_2O \rightarrow CO + H_2$	$3.42\,T$ (m s^{-1})	130	10940
Water drying : [22]				
7	H_2O (l,free) → H_2O (g)	5.13×10^8	88	2440
8	H_2O (l,bound) → H_2O (g)	5.13×10^8	88	2440

Reaction kinetic parameters that were used for the current simulation are summarized in Table 8. Other data on particle properties can be found in **Paper I**.

6.1.1. Model assessment

6.1.1.1. Grid-independent study

Finding an optimum collocation point is crucial in order to avoid unnecessary excessive usage without producing significant improvement in prediction. The grid-independent study was performed by comparing the simulation results of surface temperature, center temperature, and mass evolution, using different numbers of collocation points, i.e. from two to six points, as presented in Figure 11. The results using PDE solver is presented here as a benchmark for true solution, as it relies on employing 200 computational grid points.

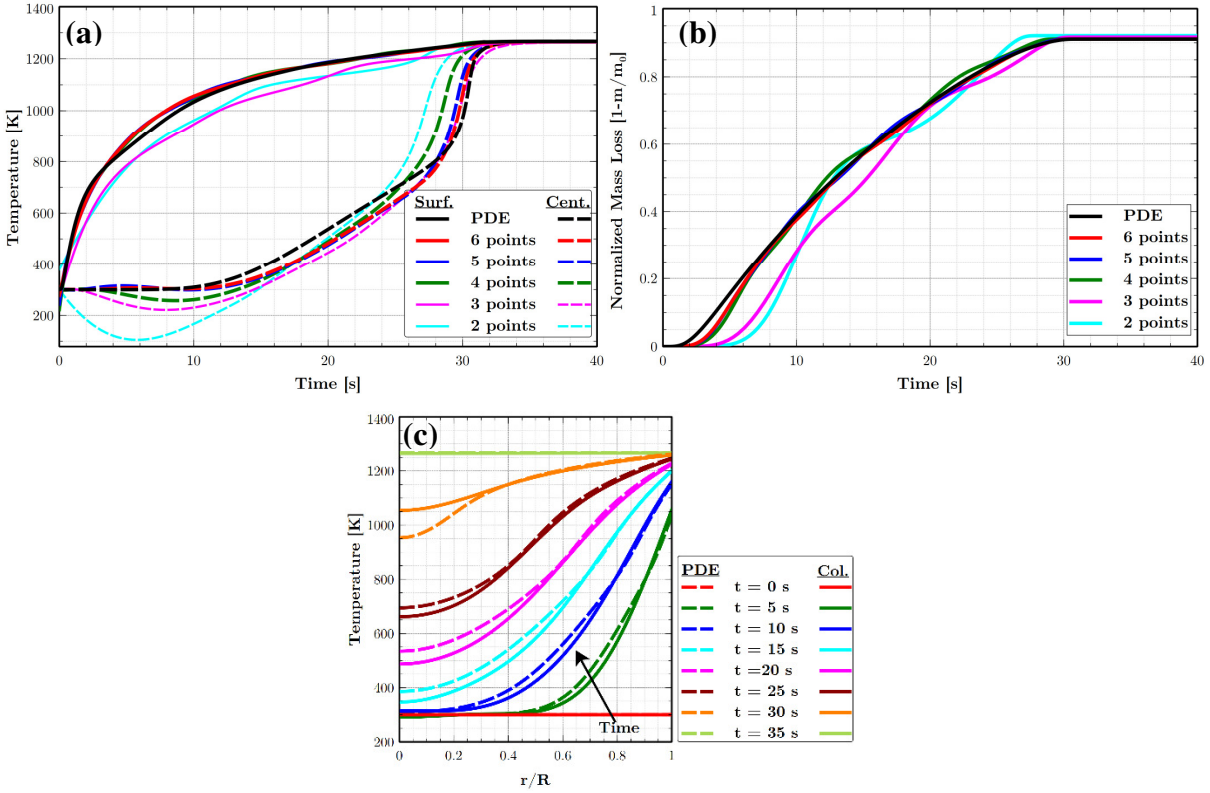

Figure 11. Mesh independency test for simulation using 9.5 mm diameter spherical particle, (a) temperature profile (b) normalized mass loss profile for different collocation point simulations (c) simulation of temperature history comparison through particle radius between PDE solver and six collocation points.

Simulation with more collocation points produced predictions that were closer to the PDE solver results. Utilization of six collocation points produced the highest degree of agreement with the PDE solver result in terms of spatial temperature history, as presented in Figure 11**c**. The utilization of more than four collocation points was found to produce insignificant improvement in the simulation results, as shown in Figure 11a and b. Four collocation points is the optimum

number of points to produce the mesh independent result for 9.5 mm diameter spherical particle simulation, as used in model validation cases. However, six collocation points were used for the rest of the analysis, which gives a margin for higher activation energies simulation that cause narrower reaction zones inside the particle. Efficiency was maintained since the computational time did not increase drastically using six collocation points.

6.1.1.2. Source term evaluation

This section presents comparisons of simulation results with and without improved resolution of reaction rate using the mass weighted average method in Eq.(64). Two different kinetics schemes and kinetics parameters were employed. Figure 12a shows the results for calculations with and without improved resolution using the global kinetic scheme or the reaction index 0 in

Table 8, using 9.5 mm diameter spherical particle. Figure 12b shows three independent parallel reaction schemes, or reaction indexes 1 to 3, with 5 mm diameter spherical particle.

The mass evolution results without improved resolution simulation are observed to be less smooth profile, as presented in Figure 12a and even worse in Figure 12b. This was due to the much higher activation energy. Less smooth behaviors are observed due to the wide distance of each collocation point to cover a very narrow reaction rate band. The less smooth profile became very prominent when the devolatilization reached the inner collocation points where the distance between the points was wider.

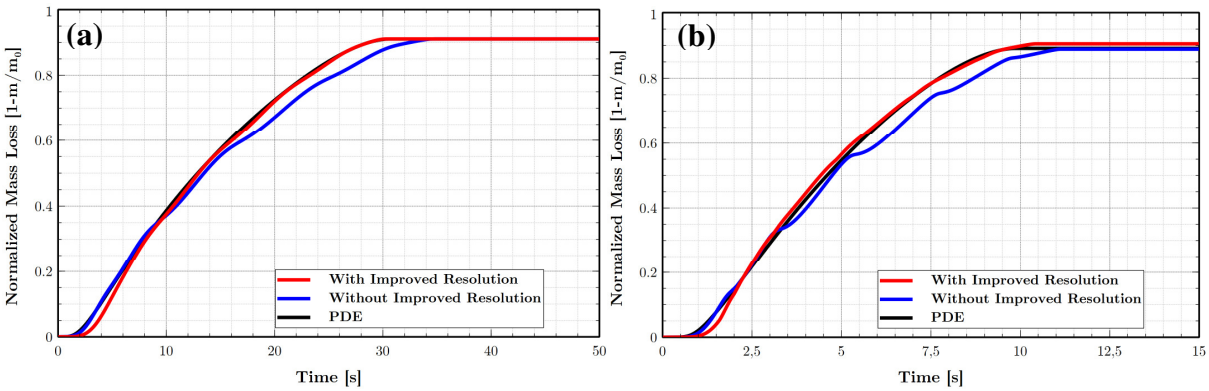

Figure 12. Normalized mass loss results with and without improved resolution of reaction rate using Eq.(64) (a) with global kinetic scheme (low activation energy) and (b) three parallel independent reaction schemes (high activation energy).

Discretization by orthogonal collocation does not automatically calculate the reaction that occurs between collocation points. This may produce sudden changes in mass loss derivative when the reaction occurs very fast at one collocation point but the temperature is not sufficient to start the reaction at the next inner point. This effect was found to be more prominent in higher

activation energy. The problem can be solved by employing more collocation points, which would consequently increase the computational effort.

An alternative used in this work with an insignificant increase in computational effort expands the coverage of reaction area and calculates the mass weighted reaction rate following Eq.(64). Based on Figure 12, the results without improved resolution provide worse agreement with the results from PDE solver compared to the results with improved resolution. This method was proven to diminish the less smooth profile in the mass loss profile and simultaneously improve the accuracy of the prediction, by better agreement with the results from PDE solver. This method was proven to diminish the less smooth profile in the mass loss profile and simultaneously improve the accuracy of the prediction, by better agreement with the results from PDE solver. This analysis also shows the applicability of the combination of the orthogonal collocation method with the current improved resolution method for any arbitrary kinetic reaction, i.e. for the complete range of activation energy found in the literature.

6.1.1.3. Moving coordinate

The importance of including the moving coordinate term in shrinking particle modelling is presented in Figure 13. This figure summarizes the simulation result for combustion case of 9.5 mm diameter spherical particle with and without a moving coordinate. The inclusion of a moving coordinate term produced a slightly faster prediction of mass loss, as expected. Without the inclusion of a moving coordinate, the fix coordinate would receive the wrong properties, which would slightly underestimate heat transport and, consequently, predict slower particle combustion.

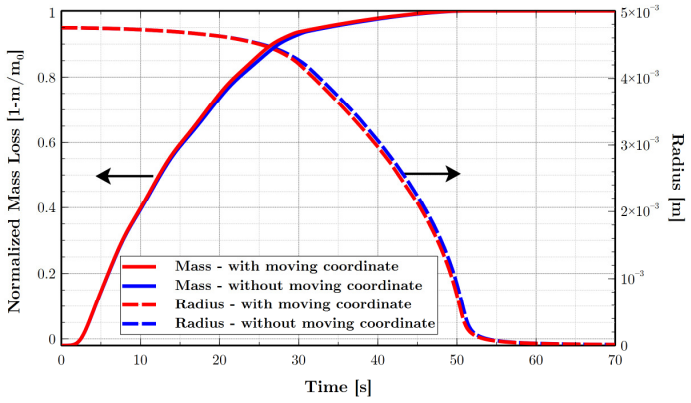

Figure 13. Comparison of normalized mass loss and radius evolution results between simulation with and without moving coordinate term for combustion case of 9.5 mm diameter spherical particle.

As shown in Figure 13, the difference between with and without moving coordinate inclusion simulation results is insignificant considering the very minor difference in predicted mass and radius evolution. This finding is due to the small temperature gradient seen when the particle started to shrink. In Eq. (62) , the $\partial T/\partial x$ term cancelled $\partial R/\partial t$, which produced an insignificant change

in temperature and the prediction of mass evolution for simulations with and without a moving coordinate. Therefore, this effect was neglected in the present study.

6.1.1.4. Stefan flow effect

Simulation result in Figure 14 display the significance of the inclusion of the effect of Stefan flow on the model in terms of global prediction of mass and radius evolution. The Sherwood number correction due to the Stefan flow from Michaelides in Eq.(46) was employed. It is assumed the material is isotropic allowing an even flow of gas through the boundary layer, while in reality the flow can be larger in the fiber direction and also effected by intermittent bursts due to cracks in the material.

The effect of Stefan flow caused a slower particle combustion time as a consequence of the reduction of the char reaction rate. The effect of Stefan flow on convective heat flux was found to be very minor due to the domination of radiative heat transfer from wall to particle, which is not affected by Stefan flow.

The major contribution of the Stefan flow effect started to occur when the particle surface reached the char reaction temperature (about 800 K) at t>5 s. The effect of Stefan flow hindered the oxidative gas from penetrating into the particle surface boundary layer. Since the exothermic char reaction has almost as strong an influence as the contribution from radiation heat, the reduction in the char reaction rate had a major impact on the total. Based on this assessment, it can be concluded that the inclusion of Stefan flow in particle combustion cannot be neglected.

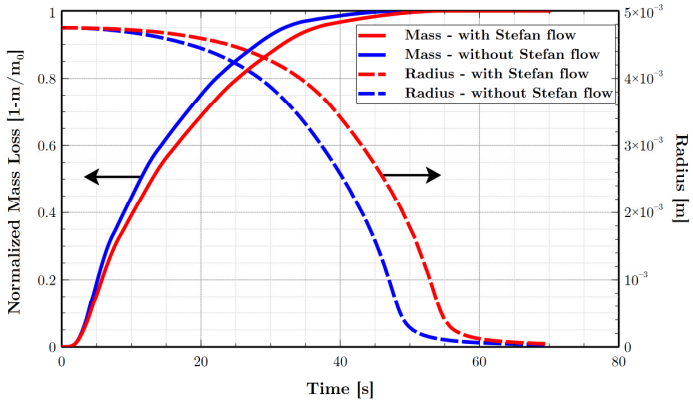

Figure 14. Comparison of normalized mass loss and radius evolution results between simulations with and without the Stefan flow effect of 9.5 mm diameter spherical particle combustion and Anderson number evolution during simulation with Stefan flow effect term inclusion.

6.1.2. Model validation

6.1.2.1. Pyrolysis experiment

A comparison of the present simulation with pyrolysis experiment is plotted in Figure 15a-d. Particle surface temperature, particle center temperature, and mass evolution during conversion were selected as the criteria to evaluate the agreement between simulated and experimental findings.

Figure 15a shows that the mass loss evolution simulation results produced very good agreement with the experimental data. The mass loss evolution of different particle characteristics was also predicted in the correct manner. The dry spherical particle displayed faster mass reduction than the dry cylinder particle and the wet cylinder particle. Additionally, both dry particles leveled out at lower values of mass loss than the moist particle, as expected.

In terms of temperature prediction, the only major discrepancy was found in the prediction of the center temperature, see Figure 15b. The experimental literature [19] has described the challenge of measuring the center temperature of a spherical particle in an accurate way. Unreasonable center temperature measurement is believed to be caused by lateral heat conduction from the outer parts of the thermocouple, which contributes to a faster increase in center temperature measurement.

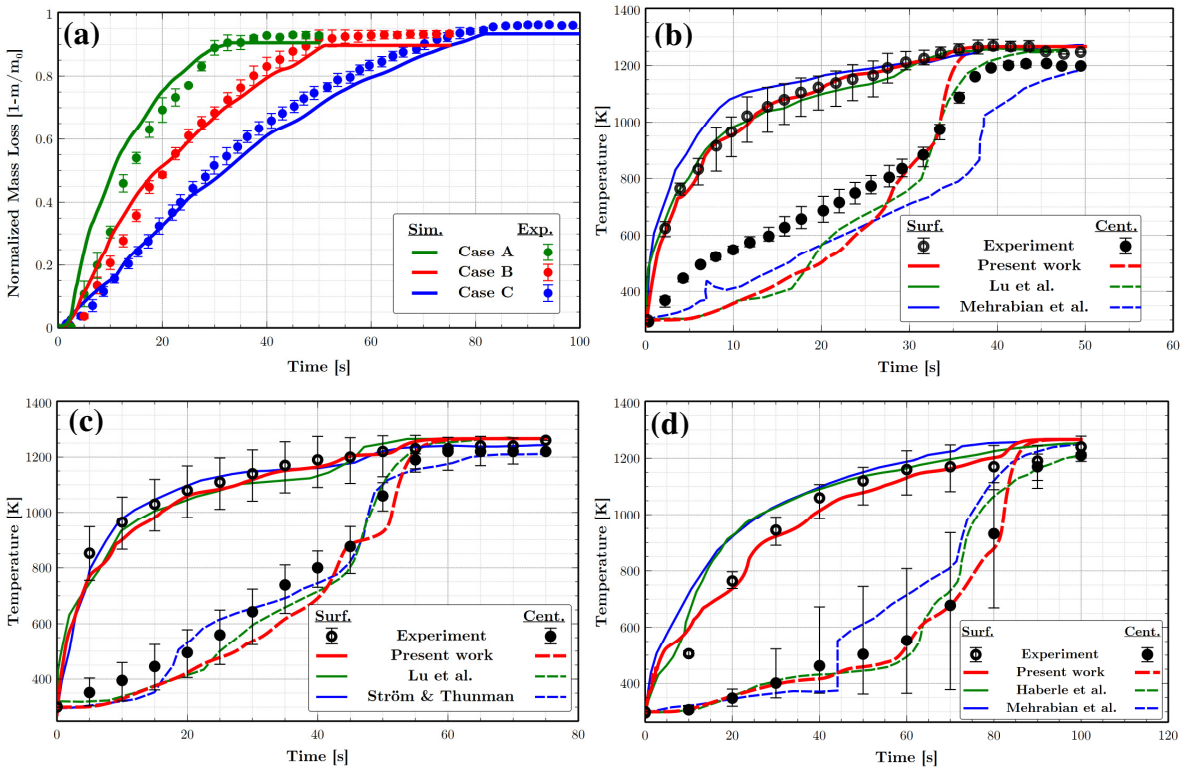

Figure 15. Comparison between simulated and measured (a) normalized mass loss of Case A, B, and C experimental data, (b) temperature from Case A experimental data, (c) temperature from Case B experimental data, and (d) temperature from Case C experimental data.

The mesh-based model is the most sophisticated model and is expected to produce more accurate results because it uses many more computational grids than the orthogonal collocation-based model and the interface-based model. However, the comparison provided in Figure 15b to d indicates that simulation accuracy can be maintained by using the orthogonal collocation method. The comparison with previous simulations leads to the conclusion that the current simulation produced almost similar temperature prediction with the mesh-based and the interface-based simulation works. These results are promising considering that the present study does not rely on tuning physical parameters and that the surface boundary condition is determined directly from the balance equation of convection, conduction and radiation at the particle surface. In some published studies, physical model parameters have been tuned e.g. heat of devolatilization and shrinkage factor, and occasionally experimentally determined surface temperature has been used as boundary condition to improve the simulation result. Notably, the experimental uncertainties for temperature measurements were fairly large as indicated by the large error bars which makes it difficult to judge which of the models agrees best.

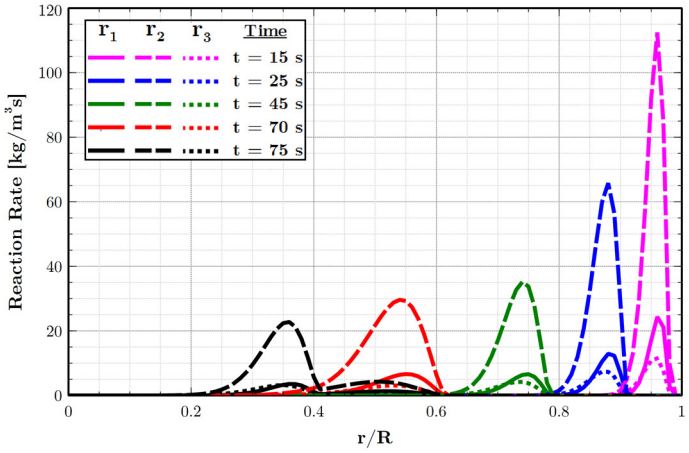

Figure 16. Simulation history of the devolatilization reaction rate over particle radius (indexes 1, 2, and 3 are referred to reaction indexes).

Analysis of the reaction rate distribution inside the particle reveals that reactions occurred in a narrow region. Figure 16 shows that the reaction zones were distributed initially around 5% and, at later stages, up to 20% of the particle radius. This wide range of devolatilization reaction zones was found especially in the early phase of the devolatilization stage when the temperature had not exceeded 700 K. The Pyrolysis number at this stage was found to be much more than 1, which physically indicates that the reaction proceeded slower than the temperature wave [69]. In the higher temperature region, the Pyrolysis number shifted to lower than 1, which implies the applicability of sharp interface models in that region.

6.1.2.2. Combustion experiment

The simulation results from particle combustion case are presented in Figure 17a and b. The results of surface temperature, center temperature, and normalized mass loss as a function of time are shown as a comparison with experimental data in Figure 17. Normalized mass loss prediction from the simulation, nearly produced overlap results with the experimental data.

Major discrepancies were found in the prediction of center and surface temperatures, see Figure 17a. As previously described in Section 6.1.2.1, the disagreement in center temperature arises primarily from the inaccuracy of the thermocouple measurement. The surface thermocouple did not measure the correct temperature since the particle had started to shrink while the thermocouple bead remained at its fixed position. After the particle started to shrink, the surface thermocouple measured the gases around the particle instead of its surface.

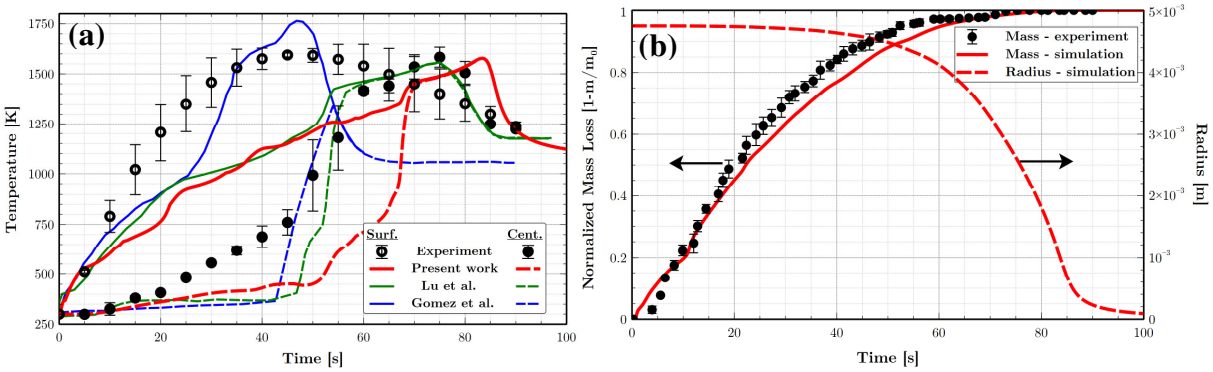

Figure 17. Comparison between simulation results and experimental data from Case D experimental data, (a) temperature (b) normalized mass loss and radius evolution.

Compared with previous simulations, the mesh-based simulation results from Lu et al [19] produced results similar to the collocation method. The interface-based model simulation by Gomez et al. [70] produced significant offset compared to the experimental results and a very different prediction compared to the two other simulation methods. Mass evolution is a more reliable for model validation considering the significantly lower error bars for mass evolution than for temperature measurements and issues related to temperature measurements. The interface model predicted that the particle would be burnt after 50 seconds instead of the 80 seconds predicted using the other methods. In other words, only the mesh-based and collocation methods accurately predicted the time for the particle to burn.

A sensitivity analysis of the shrinkage factors due to drying and devolatilization was performed and summarized in Figure 18. The shrinkage factors due to drying and devolatilization are accounted for in the model by the parameters β_m and β_b in Eq. (8). Different values of the shrinkage factors were selected based on values proposed in the literature i.e. 20% [19], 25% [22], and 50% [16]. In this current analysis the proposed values were used only as shrinkage parameter

due to devolatilization (β_b). The analysis shows faster particle conversion the higher the value of the shrinkage factor. As shown in Figure 18, 20% shrinkage gave better result compared to the nominal case without particle shrinkage.

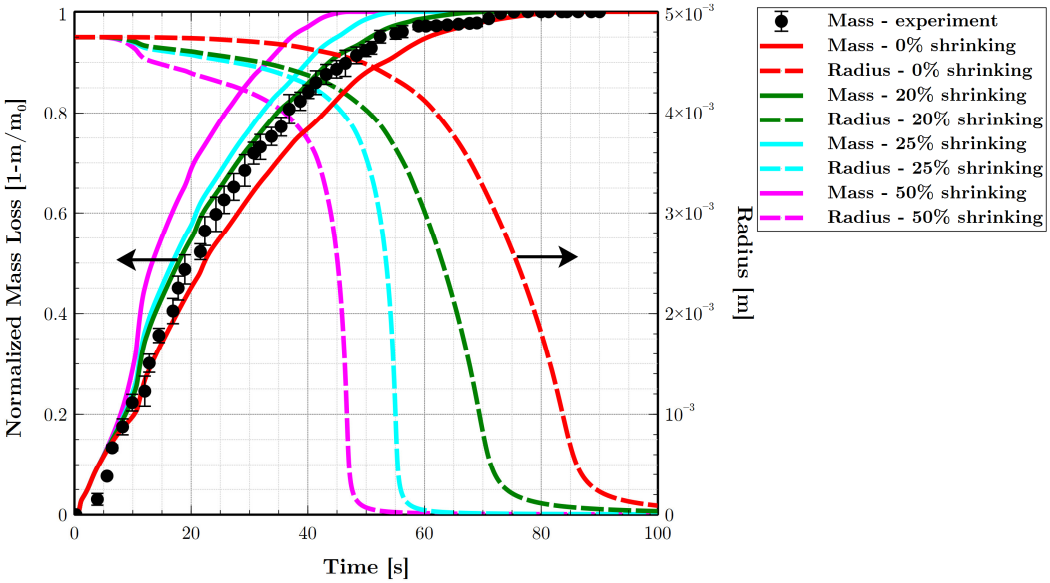

Figure 18. Sensitivity analysis of particle shrinkage.

The sensitivity analysis shows the importance of including particle shrinkage in the analysis, and it also confirms that the model is numerically stable over the range of shrinkage parameters used in the literature. The significant effect of particle shrinkage also mean that the particle shrinkage should be carefully studied while conducting single particle experiments to avoid the shrinking factor is used as tuning parameter in simulations.

6.1.3. Model efficiency

The simulation time was recorded and compared with other works to give guidance on the cost of implementing the new particle model. This is an important factor in judging if the particle model can be implemented as a sub-grid function in a CFD analysis. The simulation time in the present study depended on the number of collocation points and was in the order of seconds, but the time can be further improved by code optimization and compilation.

A previous study using the mesh-based discretization method recorded that at least 2930 seconds (48 minutes) were required to simulate experimental Case B [19]. The results indicate approximately three orders of magnitude faster simulations, while maintaining a similar accuracy as obtained in mesh-based model. The short simulation time needed in the present study was promising in that a single particle can be implemented in a CFD analysis to describe a bed of particles, which allows full coupling with local gas flow and the temperature surrounding the particles.

6.2. Sherwood number correction

6.2.1. Mesh-independent test

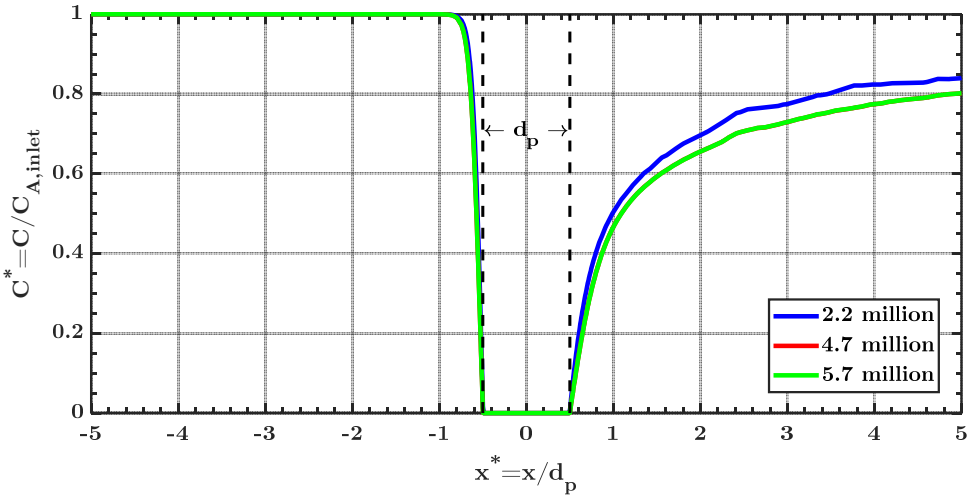

Figure 19. Mesh independence visualized by the concentration profiles in front and behind particle.

Mesh-independent test was conducted with the thinnest boundary layer condition of whole simulations which observed to be the simulation with the highest Re number and the lowest An number. The thinnest boundary layer produced the steepest gradients of concentration profile or the toughest simulation condition. The mesh independence was evaluated from the concentration gradient around the particle and the calculated Sherwood number of different mesh resolutions. A nominal mesh, 2.2 million cells, were subsequently refined to 4.7 and 5.7 million cells, by mesh adaption in regions with large gradients of species. As shown in Figure 19, the red and green lines overlap completely which confirmed that mesh-independent was reached at 4.7 million cells. Moreover, no difference in the calculated Sherwood numbers were obtained for 4.7 and 5.7 million cells.

6.2.2. Sherwood number correction without Stefan flow

A new model was derived to be fitted with the CFD simulations results. A new Sherwood number without Stefan flow follows Eq.(74).

$$Sh = 2 + 0.63\, Re^{0.51} Sc^{0.41} \tag{74}$$

This new model gave a significantly better fit compared to CFD simulation data as seen in Figure 20 and small relative error as presented in Figure 21.

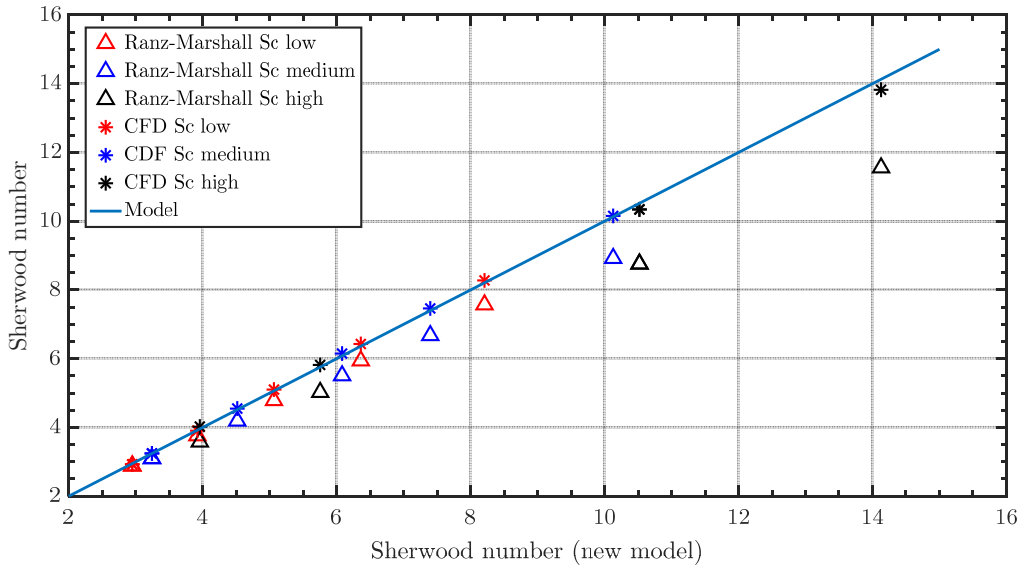

Figure 20. Comparison between the new model results (the solid line), CFD simulation results and Ranz-Marshall correlation in Eq.(22) in different range of Sc numbers (Low: 0.5<Sc<0.6 ; Medium: Sc=1.5 ;High: 2.88<Sc<=3

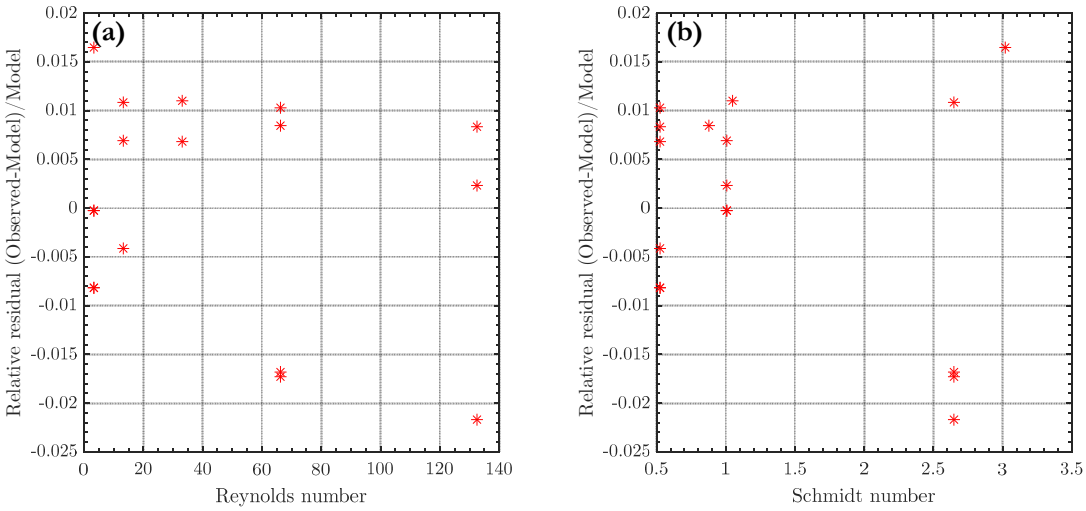

Figure 21. Residual analysis (CFD simulations-predicted Sh numbers) a) as function of Reynold number and b) as function of Schmidt number.

6.2.3.Sherwood number correction due to Stefan flow

In this sub-section, the validation of the analytical solution of Sherwood number correction due to Stefan flow is compared with the CFD simulation results. The simulations and calculations were conducted for different Schmidt, Andersson, and Reynolds numbers. Two classical Sherwood number corrections due to Stefan flow are also presented, i.e. the Spalding and Michaelides correlations.

The analytical solution of Sherwood number correction due to Stefan flow from Eq.(41) which were combined with nominal Sherwood number in Eq.(74), produced very good agreement with CFD analysis result as shown in Figure 22a. The residual was observed to increase for larger Stefan flow, as shown in Figure 22b. The residual increase was observed due to the assumption of constant film layer thickness which was used by analytical solution. The film thickness was observed to change due to Stefan flow as displayed in concentration profile of component A in Figure 23.

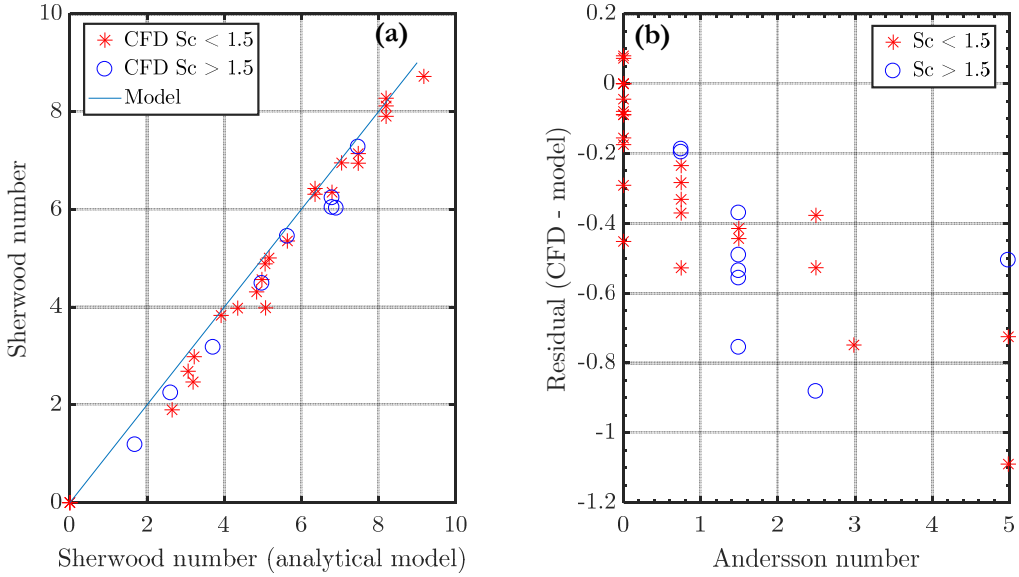

Figure 22. (a) Effective Sherwood number comparison and (b) residual value from CFD simulations vs the analytical model Eq.(41) with Sh calculated from Eq.(74) (constant film thickness layer assumption).

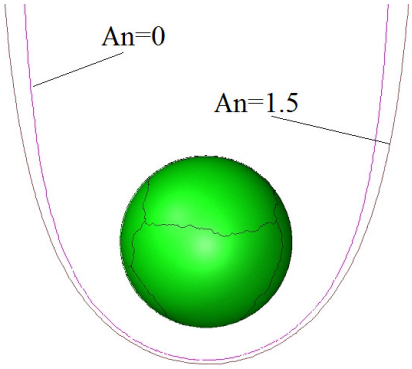

Figure 23. Contours of concentration of $C_A = 0.95C_{A,bulk}$ with and without Stefan flow.

Some adjustments to the model were performed to enhance the agreement of current analytical solution results with the CFD simulation results. The first adjustment was using the adjusted Reynolds number in Eq.(44), instead of nominal Reynolds number to calculate nominal Sherwood number in Eq.(22). The second adjustment was using the improved nominal Sherwood number as shown in Eq.(75).

$$Sh = 2 + 0.63\, Re_{p,adj}^{0.52}\, Sc^{0.41} - 0.18\, An/Sc^{0.25} \tag{75}$$

The adjustments produced even better result as shown by Figure 24a The residuals are observed to be even lower compared to the previous simulation without any adjustment as shown in Figure 24b.

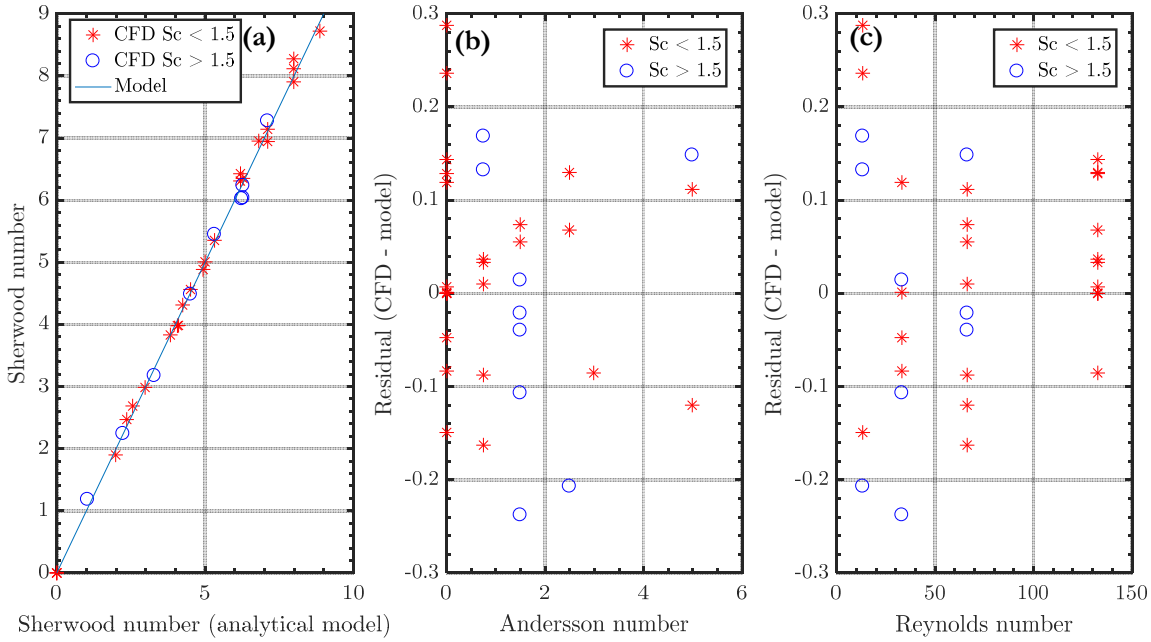

Figure 24. (a) Sherwood number comparison, (b) residual value as function of An and (c) residual value as function of Re from CFD simulations vs the analytical model Eq.(41) with adjusted Reynolds number and Sh calculated from Eq.(75).

Figure 25 presents a comparison of the current analytical solutions with CFD results and the Spalding and Michaelides correlations. The current analytical solution which was combined with some adjustments due to increased film thickness, provides much better agreement with CFD result than the other two correlations based on Figure 25. This result confirms the reliability of the current analytical solution when used for Sherwood number correction due to Stefan flow effect in the range of $Re_p < 150; 0 < Sc < 3$ and $An < 5$.

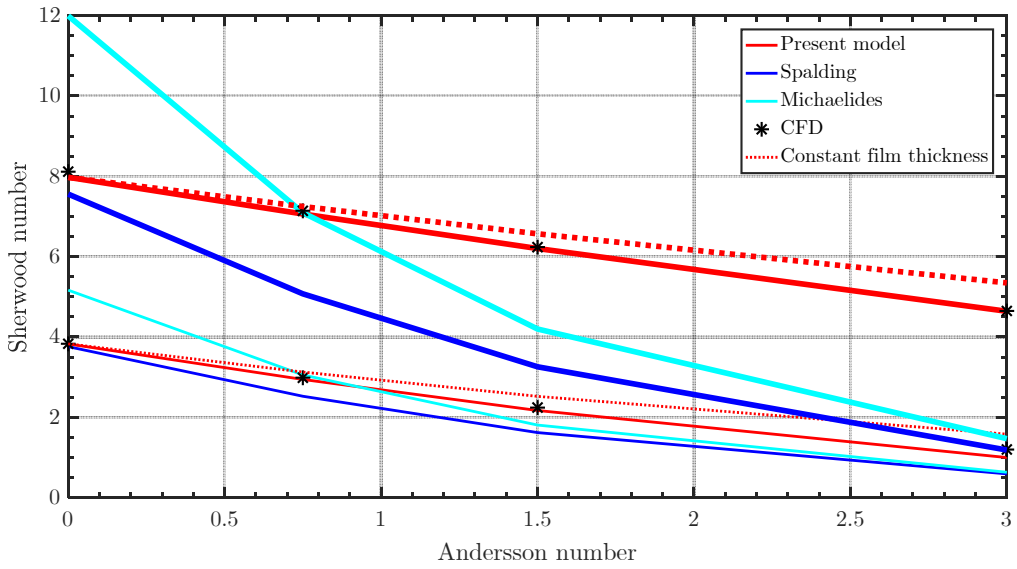

Figure 25. Comparison of different Sherwood number corrections for simulation of particle combustion, Case D. The thin lines are for Re=13 and thick lines for Re=132.

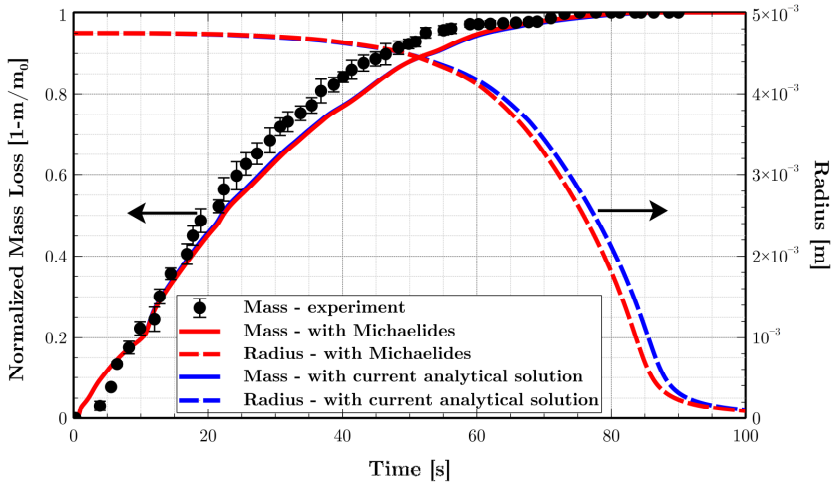

Figure 26. Comparison of utilization of Sherwood number correction from Michaelides correlation with current analytical solution to simulate Case D experimental conditions.

The applicability of the novel analytical solution for the Sherwood number due to Stefan flow was tested in particle model, and it produced the results presented in Figure 26 for Case D simulation. The particle Reynolds number for Case D was observed to be lower than 15 and the Schmidt number was observed to be in range of 0.55 to 0.6. The Andersson number was obtained to be lower than 3. These Case D simulation properties confirmed the applicability of current analytical solution.

Based on Figure 26, the stability of the implementation of the current analytical solution was proven. The difference between current analytical solution results compared to the simulation results using the Michaelides correlation, were found to be minor. This minor difference was obtained due to small particle Reynolds and Andersson number in the Case D simulation. The

Michaelides and current analytical correlation also displayed small difference in small Re_p and An numbers as shown in Figure 25.

6.3. Biomass combustion in a grate furnace

Some results from the combustion experiment in the constructed grate furnace are presented in this subsection. The main objective of the discussion is to highlight the achievements in terms of experimental stability and repeatability. Qualitative and quantitative analyses based on temperature and exhaust gas measurement results are also presented to test the reliability of the experimental method and apparatus.

6.3.1. Steady-state operation

In order to achieve consistent results in combustion modelling and PM formation analysis, steady state operation of a grate furnace was conducted. The steady state operation of constructed biomass is indicated by stable measurements of average temperature and exhaust gas composition. Figure 27 displays the history of one of the temperature measurements from the thermocouple at position 145 cm B in the current combustion experiment. Different operation stages during the experiment were found in the temperature history.

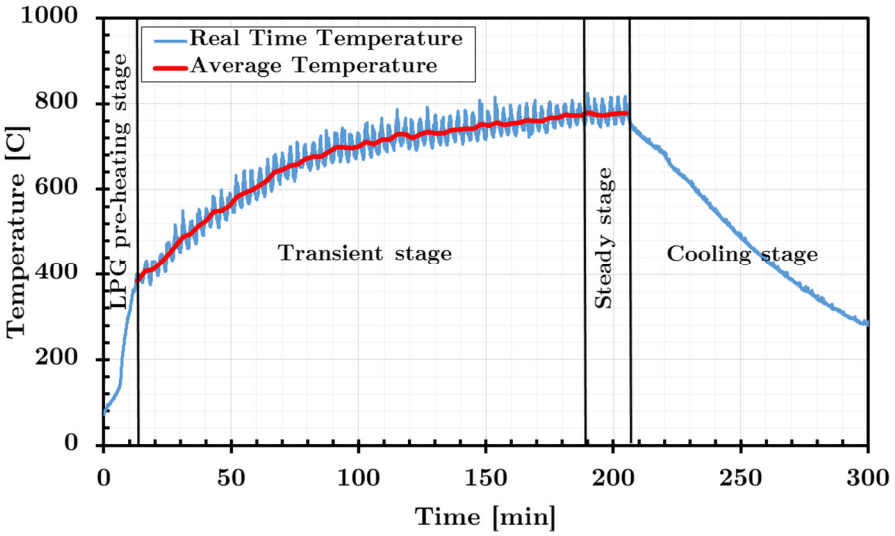

Figure 27. Temperature measurement profile at 145 cm B thermocouple and different stages of combustion experiment in grate furnace.

The experiment started with a heating up process using LPG until the biomass above the grate was ignited. The process continued using the transient stage by semi-continuous loading of 1 kg biomass every three minutes. Temperature fluctuation from one biomass reloading to the next was observed as a consequence of this reloading mechanism. The very long time of the transient stage was necessary due to the thermal mass of the furnace wall. Most of the heat produced in the transient stage by solid and gas combustion was employed to increase the temperature of the

approximately 800 kg steel wall. The average temperature slope decreased over time, and direct observation of the average temperature profile during the experiment determined whether steady state operation had been achieved or not. Figure 28a to c describe the accuracy of the steady-state operation decision with almost constant measurement of the average temperature profile in the freeboard and at the furnace wall during last three batches of biomass reloading. The achievement of steady state operation also proven by stable average $\%O_2$ measurement for the last three biomass reloading periods, as shown in Figure 28d.

6.3.2. Analysis of temperature and evolution of exhaust gas composition

Qualitative and quantitative analyses of the behavior of biomass combustion in the grate furnace is presented in this section. The consistency of different batches of experiments is shown by the stable measurements of temperature and exhaust gas composition for two different experimental batches. The consistency of the temperature measurement was demonstrated by only ± 2% error or it correspond to ± 15°C difference for the x coordinate, the z coordinate, and the average wall temperatures between the two experiments. A high degree of consistency was even more prominent in measurements of oxygen composition with about ±0.8 %vol error between each experimental batch. This repeatability of average temperature and oxygen composition measurements gave good confidence in the stability and accuracy of the results that was produced by the experimental furnace.

Figure 28a shows the uniformity of temperature distribution over the x coordinate based on a small deviation of the average measurements of the A, B, and C thermocouples. The uniformity over the x axis indicates good flow distribution of primary air over the biomass bed.

The temperature evolution of the z coordinate also gave a good temperature trend. The closest thermocouple from the biomass bed, the 60 cm thermocouple, showed the highest temperature measurement. This is due to the gas combustion was observed to occur very close to the solid biomass bed. Gas combustion is easy to observe visually by the presence of the flame, which is located right above the biomass bed. Further mixing of cooler air with hot gases produced a significant reduction of gas temperature in the higher level of the freeboard. It was well reflected in the thermocouple measurements by the lower temperature found for the higher positioned thermocouple. The reverse temperature trend was observed between the 145 cm thermocouple and the 175 cm thermocouple, which is believed to be due to gas recirculation that influences the gas mixing in the high level of the freeboard. CFD analysis can be a powerful tool to describe the phenomena that happened at this level, which is planned to be performed in future work.

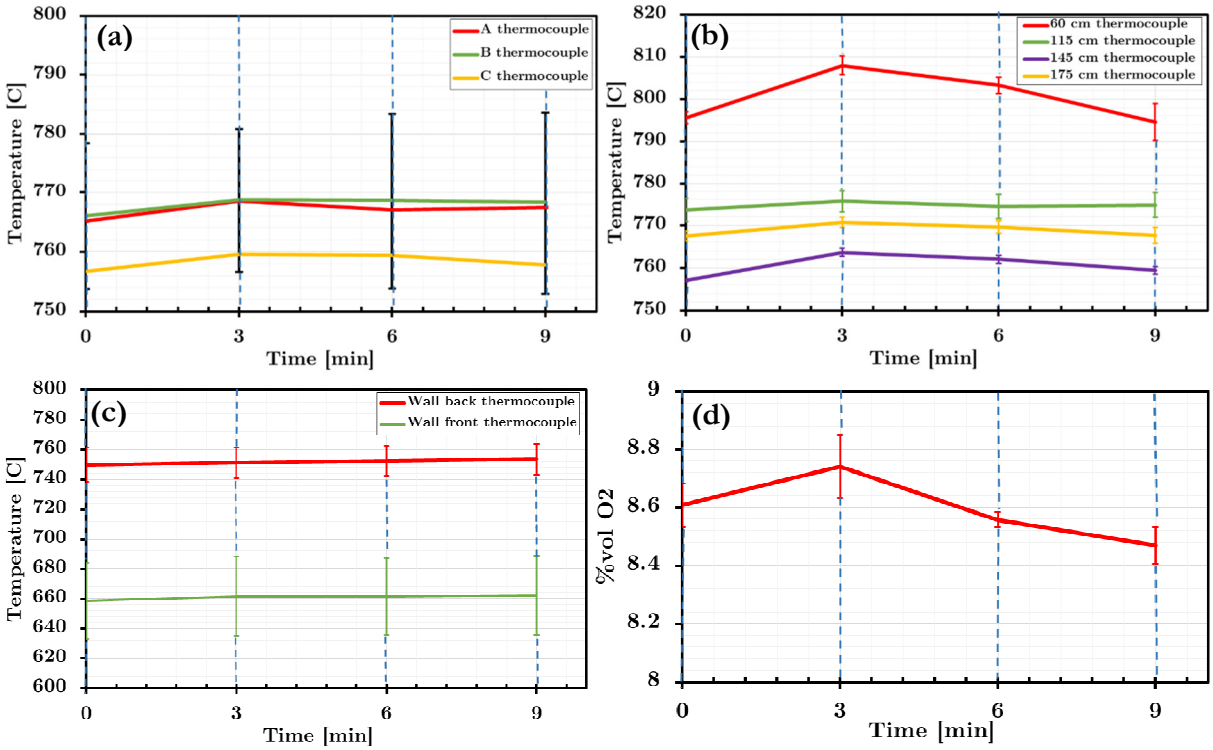

Figure 28. Profile of (a) x coordinate average temperature, (b) z coordinate average temperature (c) wall average temperature, and (d) average oxygen composition in the chimney for two different batch experiments with three reloading periods. Dashed blue line (- - -) denotes a reloading period.

Wall temperature measurements between the two experiments were found to be in good agreement. The back-wall temperature was higher than the front wall temperature, which shows the non-uniformity of the temperature in the y coordinate. This non-uniformity was expected since only 25% of the grate opening was used in the experimental setup. The remaining 75% was closed with covered metal, which made the primary air flow through 25% of the grate area. The recirculation of gas was also expected to play a role in the current non-uniformity.

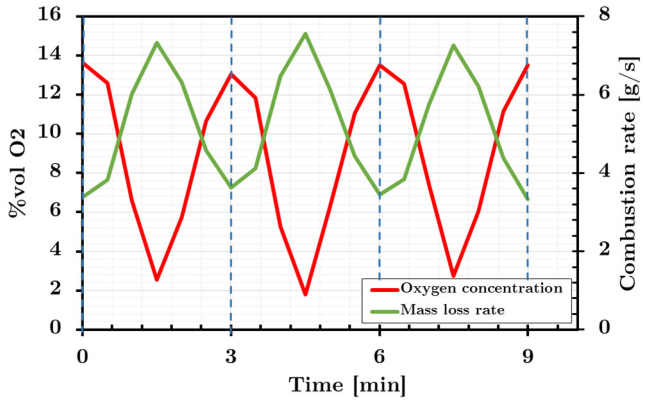

Figure 29. Oxygen composition of exhaust gas and profile of biomass mass loss rate during the last three reloading periods. Dashed blue line (- - -) denotes reloading period.

Quantitative analysis based on oxygen composition measurements was performed by evaluating the global mass balance from biomass combustion. Based on ultimate analysis of coconut shell, the coconut shell can be represented by current chemical species, $CH_{1.57}O_{0.71}$. Considering a complete biomass reaction, one mole biomass needs about 1.03 mole of oxygen to produce one mole of CO_2 based on this global reaction scheme.

$$CH_{1.57}O_{0.71} + 1.03\ O_2 \rightarrow CO_2 + 0.78\ H_2O$$

Based on the reaction scheme above, biomass decomposition rate was performed using simple global mass balance. Figure 29 shows the evolution of the rate of biomass mass loss during last three reloading periods. The average rate of total mass loss for one reloading period or during three minutes was recorded as about 0.93 kg or about 93% of the total mass inserted at every reloading. This data indicates that all biomass that was inserted during this period had decomposed completely during the three minutes. The remaining 6% came from the moisture content based on the proximate analysis shown in Table 6. This analysis revealed the steady-state behavior of the experimental setup with the furnace, which converted 100% biomass during one reloading period.

Improvement of the thermocouple measurement using two-thermocouple method gave a more correct reading of the gas temperature. As has been mentioned sub-section two-thermocouple method, the measurement of gas temperature can be affected by radiative heating or the cooling of the thermocouple bead from or to the furnace wall. The current improvement in temperature reading utilized two different thermocouples with different diameter sizes, i.e. 0.8 mm and 1.5 mm. Figure 30 presents a comparison of temperature measurements with and without correction for the radiation effect.

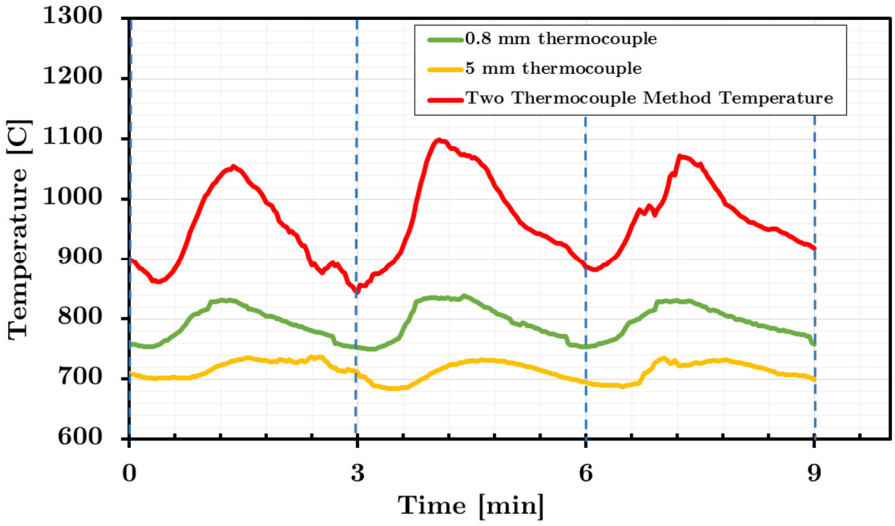

Figure 30. Gas temperature profile evolution with and without correction for radiative effect using two thermocouple methods. Dashed blue line (- - -) refers to reloading period.

Temperature measurement with larger diameter size thermocouple produced lower temperature prediction as expected. This is due to different effect of convective and radiative heating which are experienced by two different size thermocouples. The higher thermal mass in the larger thermocouple produced a slight delay in temperature reading compared to the smaller thermocouple. Figure 30 shows that gas temperature was calculated to be about 100-150°C higher than the measurement of the thin thermocouple. This corrected temperature is much closer to the temperature predicted using the global heat balance analysis, which predicted about 1300°C at the current biomass combustion rate.

There is still about 300°C difference between the value from experimental compared to the value from global heat balance calculations. This difference can be attributed due to the effect of excluding gas radiation to the thermocouple bead and the exclusion of accumulation term in two thermocouple calculations. The difference can be due to the non-uniformity of temperature inside the furnace, which causes an inaccuracy in the selection of material properties and boundary conditions when calculating the global heat balance. The minor increase in wall temperature, as shown Figure 28c, might also be attributed to an inaccuracy in the calculation since a very large thermal mass is contributed by the furnace wall. A more advanced assessment would give a more correct prediction of the current combustion behavior, i.e. using CFD analysis, which is planned for future work.

7. CONCLUSIONS AND OUTLOOK

In order to develop knowledge of PM reduction in biomass combustion system, experimental and modelling works have been performed. An experimental grate furnace was designed and constructed, and combustion experiments were performed to test the stability of the furnace. Two main modelling works were performed in this current work in order to produce accurate and efficient biomass particle combustion and accurate PM precursors release prediction. The modelling works were consisted of the evaluation of Stefan flow effect on heat and mass transfer and the development of a particle model in pyrolysis and combustion condition.

The repeatability of the experimental furnace was proven by the insignificant deviation of temperature and exhaust gas measurement profiles from different batches of experiments. The observed values in the experimental setup were found to be reliable by the good trend in temperature history measurements in the x, y, and z coordinates. Two thermocouple methods were conducted to compensate the gas temperature measurement error that arises due to radiative heating or cooling. These methods produced a significant correction in gas temperature, which gave a better prediction than the global heat balance calculation.

The new models of Sherwood number with and without Stefan flow were derived in current study based on CFD simulations results. The new models of nominal Sherwood number were observed to produce better prediction than classical correlation from Ranz-Marshall. The effect of Stefan flow on heat and mass transfer was evaluated by deriving analytical solution for Sherwood and Nusselt number corrections and by considering the increased film thickness due to Stefan flow. The novel analytical solution results produced very good agreement with the CFD analysis results in the range of $Re_p < 150$; $0.5 < Sc < 3$ and $An < 5$ for spherical geometry. The current analytical solution calculation results also displayed better agreement with CFD analysis than some classical Sherwood number correction correlations, i.e. the Spalding and Michaelides correlations. Moreover, the application of current analytical correlation was proven to be stable in biomass particle combustion case.

The developed particle model for pyrolysis and combustion was constructed using the orthogonal colocation method. The discretization scheme combined with a comprehensive physicochemical particle model allowed improvement in heat and mass transfer rates inside the particle and at the particle surface. The model formulation provided great flexibility, including the incorporation of i) arbitrary reaction kinetics, ii) local varying properties, iii) heat adsorption by

evaporated gas, iv) gradient-driven transport mechanisms such as water movement by diffusion inside the biomass matrix, and v) the inclusion of the effect of Stefan flow on the heat and mass transfer rates at the particle surface.

The importance of including different physical phenomena in the model was studied. The improved resolution of the reaction rate using the mass weighted average was proven to improve the accuracy of the current particle model. The less smooth profile that was observed without improved resolution was significantly reduced using the current improvement. The inclusion of Stefan flow effect had a significant influence on the predicted mass loss and radius evolution but only for a limited time; the greatest effect was found in an intermediate time window in the period where the char reaction occurs in parallel with devolatilization and/or drying. It was found that the inclusion of the moving coordinate term is not important for the systems studied. The efficiency of the current particle model was demonstrated through the low usage of computational power. Model validation using data from particle pyrolysis and combustion experiments for different particle moisture contents and shapes confirmed that the intra-particle temperature gradient, as well as particle mass and size evolution, can be predicted accurately.

The results of this work are considered to be very promising for further implementation to realize the overall objective. The combination of the good prediction of particle modelling results and reliable data from the experimental work allows the results to be utilized further in the CFD analysis framework to simulate full furnace setup. The reliability of experimental data from the combustion furnace can be used to validate CFD analyses in the future. By combining the features of the experimental furnace that allow PM sampling with the simulation using the developed particle model, which has been proven to predict accurate particle combustion behavior and the release of PM precursors, comprehensive knowledge of PM formation in a biomass combustion system will be gained.

8. NOMENCLATURE

a	=	Coefficient for cubic hermite interpolation [-]
A	=	Pre-exponential factor [s^{-1}] ; Orthogonal collocation coefficient for first derivative [-]
An	=	Andersson number [-]
A_p	=	Particle surface area [m^2]
b	=	Coefficient for cubic hermite interpolation [-]
B	=	Orthogonal collocation coefficient for second derivative [-]
Bi	=	Biot number [-]
$const$	=	Constant for Stefan flow analytical solution derivation
c	=	Coefficient for cubic hermite interpolation [-]
C	=	Concentration [kg m^{-3}]
Cp	=	Specific heat capacity [J kg^{-1} K^{-1}]
d	=	Orthogonal collocation coefficient Coefficient for cubic hermite interpolation [-]
d_p	=	Diameter particle [m]
d_{pore}	=	Particle pore diameter [m]
D	=	Diffusivity [m^2 s^{-1}]
E_a	=	Activation energy [kJ mol^{-1}]
F	=	External body forces [kg m^{-2} s^{-2}]
g	=	Gravitational forces [m s^{-2}]
h	=	Convective heat transfer coefficient [W m^{-2} K^{-1}]
h_m	=	Convective mass transfer coefficient [m s^{-1}]
J_i	=	Diffusion flux of species i [kg m^{-3} s^{-1}]
k	=	Reaction rate constant [s^{-1}]
l	=	Thickness [m]
L	=	Length [m]
M	=	Molecular weight [kg $kmol^{-1}$]
N	=	Total collocation points [-]; Surface gas flux [kg m^{-2} s^{-1}]
Nu	=	Nusselt number [-]
p	=	Static pressure [N m^{-2}]
Pr	=	Prandtl number [-]
Q	=	Orthogonal collocation coefficient [-]
r	=	Local radius [m]
$\dot{r}$	=	Reaction rate [kg m^{-3} s^{-1}] / [kg m^{-2} s^{-1}]
R	=	Radius [m]
R_i	=	Net rate of production of species i [kg m^{-3} s^{-1}]
R_g	=	Ideal gas constant [kJ mol^{-1} K^{-1}]
Re	=	Reynolds number [-]
S_i	=	The rate of creation of species i by addition from the dispersed phase plus any user-defined sources [kg m^{-3} s^{-1}]
S_m	=	Mass added to continuous phase from the dispersed second phase and any user-defined sources [kg m^{-3} s^{-1}]
Sh	=	Sherwood number [-]
Sc	=	Schmidt number [-]
t	=	Time [s]
T	=	Temperature [K]
u	=	Velocity [m s^{-1}]
V	=	Volume [m^3]

W	=	Weighting factor in shifted Legendre polynomials
	=	Width [m]
x	=	Dimensionless coordinate [-]
Y_i	=	Local mass fraction of species i [-]

Greek Letters

ΔH	=	Heat of reaction [kJ kg^{-1}]
a	=	Geometry coefficient [-]
β	=	Shrinking and swelling factor [-]
ε	=	Porosity [-]
λ	=	Thermal conductivity [W m^{-1} K^{-1}]
ρ	=	Density or species concentration [kg m^{-3}]
$\bar{\bar{\tau}}$	=	Stress tensor [N m^{-2}]
σ	=	Emmisivity [-]
u	=	Velocity [m s^{-1}]
ω	=	Stefan-Boltzmann constant [W m^{-2} K^{-4}]
ν	=	Kinematic visosity [m^2 s^{-1}]

Subscript

0	=	Initial or nominal
ash	=	Ash
b	=	Dry biomass
		Thermocouple bead
bl	=	Boundary layer
tot	=	Cumulative properties for biomass
$bulk$	=	Bulk gas
bw	=	Bound water
c	=	Char
$char$	=	Char reaction
CO_2	=	Carbon monoxide
dev	=	Devolatilization
dry	=	Drying
eff	=	Effective properties
fw	=	Free water
g	=	Gas
H	=	Heat (refers to Andersson number for heat)
i	=	Index for reaction or collocation point location
j	=	Index for Euclidean point
k	=	Index for species or reaction
		Index for shifted Legendre polynomials
l	=	Large diameter particle
m	=	Index for shifted Legendre polynomials
$michaelides$	=	Michaelides correlation for Sherwood number correction due to Stefan flow
new	=	Updated value (related to moving coordinate)
old	=	Old value (related to moving coordinate)
$outlet$	=	Outlet of computational domain (related to CFD analysis of Sherwood number)
p	=	Particle
s	=	Area based (for reaction)
		Small diameter particle
$surf$	=	Particle surface
$spalding$	=	Spalding correlation for Sherwood number correction due to Stefan flow
v	=	Volume-based (for reaction)
$wall$	=	Reactor wall
∞	=	Surrounding conditions (two thermocouple measurements)

9. REFERENCES

[1] Zhao P, Shen Y, Ge S, Chen Z, Yoshikawa K. Clean solid biofuel production from high moisture content waste biomass employing hydrothermal treatment. Appl Energy 2014;131:345–67.

[2] Porteous A. Energy from Waste: A Wholly Acceptable Waste-management Solution. Appl Energy 1997;58:177–208.

[3] Probert SD, Kerr K, Brown J. Harnessing energy from domestic, municipal and industrial refuse. Appl Energy 1987;27:89–168.

[4] Yin C, Rosendahl LA, Kær SK. Grate-firing of biomass for heat and power production. Prog Energy Combust Sci 2008;34:725–54.

[5] Zappa W, Junginger M, van den Broek M. Is a 100% renewable European power system feasible by 2050? Appl Energy 2019;233–234:1027–50.

[6] Di Blasi C. Modeling chemical and physical processes of wood and biomass pyrolysis. Prog Energy Combust Sci 2008;34:47–90.

[7] He C, Giannis A, Wang JY. Conversion of sewage sludge to clean solid fuel using hydrothermal carbonization: Hydrochar fuel characteristics and combustion behavior. Appl Energy 2013;111:257–66.

[8] Roy MM, Corscadden KW. An experimental study of combustion and emissions of biomass briquettes in a domestic wood stove. Appl Energy 2012;99:206–12.

[9] Savolainen K. Co-firing of biomass in coal-fired utility boilers. Appl Energy 2003;74:369–81.

[10] 2030 Energy Strategy - European Commission n.d. https://ec.europa.eu/energy/en/topics/energy-strategy-and-energy-union/2030-energy-strategy (accessed December 15, 2018).

[11] Sweden to reach its 2030 renewable energy target this year | World Economic Forum n.d. https://www.weforum.org/agenda/2018/07/sweden-to-reach-its-2030-renewable-energy-target-this-year/ (accessed December 15, 2018).

[12] Nyström R, Lindgren R, Avagyan R, Westerholm R, Lundstedt S, Boman C. Influence of Wood Species and Burning Conditions on Particle Emission Characteristics in a Residential Wood Stove. Energy and Fuels 2017;31:5514–24.

[13] Sippula O. Fine particle formation and emission in biomass combustion. University of Eastern Finland, 2010.

[14] Josephson AJ, Linn RR, Lignell DO. Modeling soot formation from solid complex fuels. Combust Flame 2018;196:265–83.

[15] Sippula O, Hytönen K, Tissari J, Raunemaa T, Jokiniemi J. Effect of wood fuel on the emissions from a top-feed pellet stove. Energy and Fuels 2007;21:1151–60.

[16] Ström H, Thunman H. CFD simulations of biofuel bed conversion: A submodel for the drying and devolatilization of thermally thick wood particles. Combust Flame 2013;160:417–31.

[17] Ström H, Thunman H. A computationally efficient particle submodel for CFD-simulations of fixed-bed conversion. Appl Energy 2013;112:808–17.

[18] Bryden KM, Hagge MJ. Modeling the combined impact of moisture and char shrinkage on the pyrolysis of a biomass particle☆. Fuel 2003;82:1633–44.

[19] Lu H, Robert W, Peirce G, Ripa B, Baxter LL. Comprehensive study of biomass particle combustion. Energy and Fuels 2008;22:2826–39.

[20] Khodaei H, Yeoh GH, Guzzomi F, Porteiro J. A CFD-based comparative analysis of drying in various single biomass particles. Appl Therm Eng 2018;128:1062–73.

[21] Haberle I, Skreiberg Ø, Łazar J, Haugen NEL. Numerical models for thermochemical degradation of thermally thick woody biomass, and their application in domestic wood heating appliances and grate furnaces. Prog Energy Combust Sci 2017;63:204–52.

[22] Haberle I, Haugen NEL, Skreiberg Ø. Drying of Thermally Thick Wood Particles: A Study of the Numerical Efficiency, Accuracy, and Stability of Common Drying Models. Energy and Fuels 2017;31:13743–60.

[23] Neves D, Thunman H, Matos A, Tarelho L, Gómez-Barea A. Characterization and prediction of biomass pyrolysis products. Prog Energy Combust Sci 2011;37:611–30.

[24] Haseli Y, van Oijen JA, de Goey LPH. Modeling biomass particle pyrolysis with temperature-dependent heat of reactions. J Anal Appl Pyrolysis 2011;90:140–54.

[25] Haseli Y, Van Oijen JA, De Goey LPH. A simplified pyrolysis model of a biomass particle based on infinitesimally thin reaction front approximation. Energy and Fuels 2012;26:3230–43.

[26] Porteiro J, Granada E, Collazo J, Patino D, Moran JC. A model for the combustion of large particles of densitied wood. Energy & Fuels 2007;21:3151–9.

[27] Thunman H, Leckner B, Niklasson F, Johnsson F. Combustion of wood particles - A particle model for Eulerian calculations. Combust Flame 2002;129:30–46.

[28] Wurzenberger JC, Wallner S, Raupenstrauch H, Khinast JG. Thermal conversion of biomass: Comprehensive reactor and particle modeling. AIChE J 2002;48:2398–411.

[29] Porteiro J, Míguez JL, Granada E, Moran JC. Mathematical modelling of the combustion of a single wood particle. Fuel Process Technol 2006;87:169–75.

[30] Hagge MJ, Bryden KM. Modeling the impact of shrinkage on the pyrolysis of dry biomass. Chem Eng Sci 2002;57:2811–23.

[31] Grønli MG, Melaaen MC. Mathematical Model for Wood PyrolysisComparison of Experimental Measurements with Model Predictions. Energy & Fuels 2000;14:791–800.

[32] Bryden KM, Ragland KW, Rutland CJ. Modeling thermally thick pyrolysis of wood. Biomass and Bioenergy 2002;22:41–53.

[33] Biswas AK, Umeki K. Simplification of devolatilization models for thermally-thick particles: Differences between wood logs and pellets. Chem Eng J 2015;274:181–91.

[34] Mehrabian R, Zahirovic S, Scharler R, Obernberger I, Kleditzsch S, Wirtz S, et al. A CFD model for thermal conversion of thermally thick biomass particles. Fuel Process Technol 2012;95:96–108.

[35] Ranzi E, Cuoci A, Faravelli T, Frassoldati A, Migliavacca G, Pierucci S, et al. Chemical Kinetics of Biomass Pyrolysis. Energy & Fuels 2008;22:4292–300.

[36] Moilanen A, Saviharju K, Harju T. Steam Gasification Reactivities of Various Fuel Chars. Adv Thermochem Biomass Convers 1993:131–41.

[37] Di Blasi C. Combustion and gasification rates of lignocellulosic chars. Prog Energy Combust Sci 2009;35:121–40.

[38] Sippula O, Hokkinen J, Puustinen H, Yli-Pirilä P, Jokiniemi J. Comparison of particle emissions from small heavy fuel oil and wood-fired boilers. Atmos Environ 2009;43:4855–64.

[39] Kocbach Bølling A, Pagels J, Yttri K, Barregard L, Sallsten G, Schwarze PE, et al. Health effects of

residential wood smoke particles: the importance of combustion conditions and physicochemical particle properties. Part Fibre Toxicol 2009;6:29.

[40] Bockhorn H. Soot Formation in Combustion Mechanisms and Models. vol. 59. Springer-Verlag; 1994.

[41] Haberle I, Haugen NEL, Skreiberg Ø. Combustion of Thermally Thick Wood Particles: A Study on the Influence of Wood Particle Size on the Combustion Behavior. Energy & Fuels 2018;32:6847–62.

[42] Whitaker S. Forced Convection Heat Transfer Correlations for Flow In Pipes, Past Flat Plates, Single Spheres, and for Flow In Packed Beds and Tube Bundles. AIChE J 1972;18:361–71.

[43] Bird RB (Robert B, Stewart WE, Lightfoot EN. Transport phenomena. J. Wiley; 2007.

[44] Spalding DB (Dudley B. Combustion and mass transfer : a textbook with multiple-choice exercises for engineering students. Pergamon Press; 1979.

[45] Michaelides EE. PARTICLES, BUBBLES AND DROPS - Their Motion, Heat and Mass Transfer. World Scientific Publishing Co. Pte. Ltd.; 2006.

[46] Di Blasi C. Heat, momentum and mass transport through a shrinking biomass particle exposed to thermal radiation. Chem Eng Sci 1996;51:1121–32.

[47] Sand U, Sandberg J, Larfeldt J, Bel Fdhila R. Numerical prediction of the transport and pyrolysis in the interior and surrounding of dry and wet wood log. Appl Energy 2008;85:1208–24.

[48] Gómez MA, Porteiro J, De la Cuesta D, Patiño D, Míguez JL. Dynamic simulation of a biomass domestic boiler under thermally thick considerations. Energy Convers Manag 2017;140:260–72.

[49] Finlayson BA. Packed bed reactor analysis by orthogonal collocation. Chem Eng Sci 1971;26:1081–91.

[50] Carey GF, Finlayson BA. Orthogonal collocation on finite elements. Chem Eng Sci 1975;30:587–96.

[51] Segall NL, Macgregor JF, Wright JD. Collocation methods for solving packed bed reactor models with radial gradients. Can J Chem Eng 1984;62:808–17.

[52] Kaczmarski K, Mazzotti M, Storti G, Morbidelli M. Modeling fixed-bed adsorption columns through orthogonal collocations on moving finite elements. Comput Chem Eng 1997;21:641–60.

[53] Babu B., Sastry KK. Estimation of heat transfer parameters in a trickle-bed reactor using differential evolution and orthogonal collocation. Comput Chem Eng 1999;23:327–39.

[54] McKay G. Solution to the homogeneous surface diffusion model for batch adsorption systems using orthogonal collocation. Chem Eng J 2001;81:213–21.

[55] Skoneczny S, Cioch M. Modeling of continuous-flow bioreactors with a biofilm with the use of orthogonal collocation on finite elements. Chem Eng Commun 2018;205:1–18.

[56] Rahimpour MR, Iranshahi D, Pourazadi E, Paymooni K. Evaluation of optimum design parameters and operating conditions of axial- and radial-flow tubular naphtha reforming reactors, using the differential evolution method, considering catalyst deactivation. Energy and Fuels 2011;25:762–72.

[57] Afshar Ebrahimi A, Ebrahim HA, Jamshidi E. Solving partial differential equations of gas-solid reactions by orthogonal collocation. Comput Chem Eng 2008;32:1746–59.

[58] Bu C, Leckner B, Chen X, Gómez-Barea A, Liu D, Pallarès D. Devolatilization of a single fuel particle in a fluidized bed under oxy-combustion conditions. Part B: Modeling and comparison with measurements. Combust Flame 2015;162:809–18.

[59] Fatehi H, Bai XS. A Comprehensive Mathematical Model for Biomass Combustion. Combust Sci Technol 2014;186:574–93.

[60] Kuenne G, Avdić A, Janicka J. Assessment of subgrid interpolation for the source term evaluation within premixed combustion simulations. Combust Flame 2017;178:225–56.

[61] Rice JR, Rice JR. INTERPOLATION. Numer Methods Softw Anal 1993:93–171.

[62] Inc. ANSYS. ANSYS FLUENT Theory Guide. Release 182 2013;15317:373–464.

[63] Koppejan J, Loo S van, Loo S van. The Handbook of Biomass Combustion and Co-firing. Routledge; 2012.

[64] Brohez S, Delvosalle C, Marlair G. A two-thermocouples probe for radiation corrections of measured temperatures in compartment fires. Fire Saf J 2004;39:399–411.

[65] Akmal N, Lauer J. Electrochemical Oxygen Sensors: Principles and Applications. Polym Sensors 1998;690:149–60.

[66] Coconut production in Indonesia n.d. www.tridge.com/intelligences/coconut/ID/production (accessed December 18, 2018).

[67] Tsamba AJ, Yang W, Blasiak W. Pyrolysis characteristics and global kinetics of coconut and cashew nut shells. Fuel Process Technol 2006;87:523–30.

[68] Grønli MG. A theoretical and experimental study of the thermal degradation of biomass. ITEV-rapport 1996:115, 1996.

[69] Pyle DL, Zaror CA. Heat transfer and kinetics in the low temperature pyrolysis of solids. Chem Eng Sci 1984;39:147–58.

[70] Gómez MA, Porteiro J, Patiño D, Míguez JL. Fast-solving thermally thick model of biomass particles embedded in a CFD code for the simulation of fixed-bed burners. Energy Convers Manag 2015;105:30–44.